ABSTRACT

Development of a Dynamic Human Body Phantom Model for On-body Electromagnetic Wave Propagation and Antenna Radiation Study

George Lee, Ph.D.

Co-Mentor: Brian Garner, Ph.D.
Co-Mentor: Yang Li, Ph.D.

Wireless body area network (WBAN) technology has many valuable applications including long-term, remote health monitoring for the general population, the military, and athletes. A key challenge for practical realization of WBAN promise is minimizing electrical power requirements for wireless transmission of data, which is complicated by the presence and motion of the human wearer's body. Improving the understanding of how electromagnetic (EM) waves propagate on and around the human body is critical to guide design of power-efficient antennas for on-body wireless communication. In this dissertation an investigative approach is developed that combines experimental and computational approaches using human volunteers, a physical human phantom model, and a simulated virtual human computer model. The investigative approach incorporating the phantom model is shown to be an effective, modular tool for well-controlled parametric study of on-body EM wave propagation utilizing multiple antenna types.

Development of a Dynamic Human Body Phantom Model for On-body Electromagnetic Wave Propagation and Antenna Radiation Study

by

George Lee, B.S.M.E, M.S.M.E.

A Dissertation

Approved by the Department Mechanical Engineering

_____

Paul Ro, Ph.D., Chairperson

Submitted to the Graduate Faculty of
Baylor University in Partial Fulfillment of the
Requirements for the Degree
of

Doctor of Philosophy

Approved by the Dissertation Committee

_____

Brian Garner, Ph.D., Co-Chairperson

_____

Yang Li, Ph.D., Co-Chairperson

_____

David Jack, Ph.D.

_____

Jonathan Rylander, Ph.D.

_____

Yue Ling, Ph.D.

Accepted by the Graduate School

May 2020

_____

J. Larry Lyon, Ph.D., Dean

Page bearing signatures is kept on file in the Graduate School.

TABLE OF CONTENTS

LIST OF FIGURES

LIST OF TABLES

ACKNOWLEDGMENTS

This study was supported in part by funds from National Science Foundation grant ECCS-1609371, Baylor Scott and White Health, and Baylor University.

DEDICATION

To my supportive family and friends.

CHAPTER ONE

Introduction

Motivation

Wearable devices, ranging from medical devices to consumer electronics, are a rapidly growing field of technology that have the potential to improve human quality of life. One particular area where these devices can make a significant impact is in remote, long-term health monitoring. Wireless body area networks (WBAN) can utilize the body-worn medical sensor devices, such as a heart rate monitor or motion sensor, to record and transmit valuable health data to a physician's office over the internet via a smartphone app. This would allow medical experts to continuously observe and monitor a patient's health over time and predict or detect any medical anomalies, allowing for timely medical care to be administered. A potential implementation diagram of a WBAN system can be seen in Figure 1.1 [1].

Many studies have examined using WBAN systems for detecting falls, activity monitoring, and monitoring other health statistics [2]-[5], which have many uses in health monitoring, as well as potential military and athletic applications. Further work has been performed to implement WBAN systems to improve athletic training [6]. Additional improvements to the performance of sensors in WBAN systems will allow for more real-world applications of WBAN to be implemented.

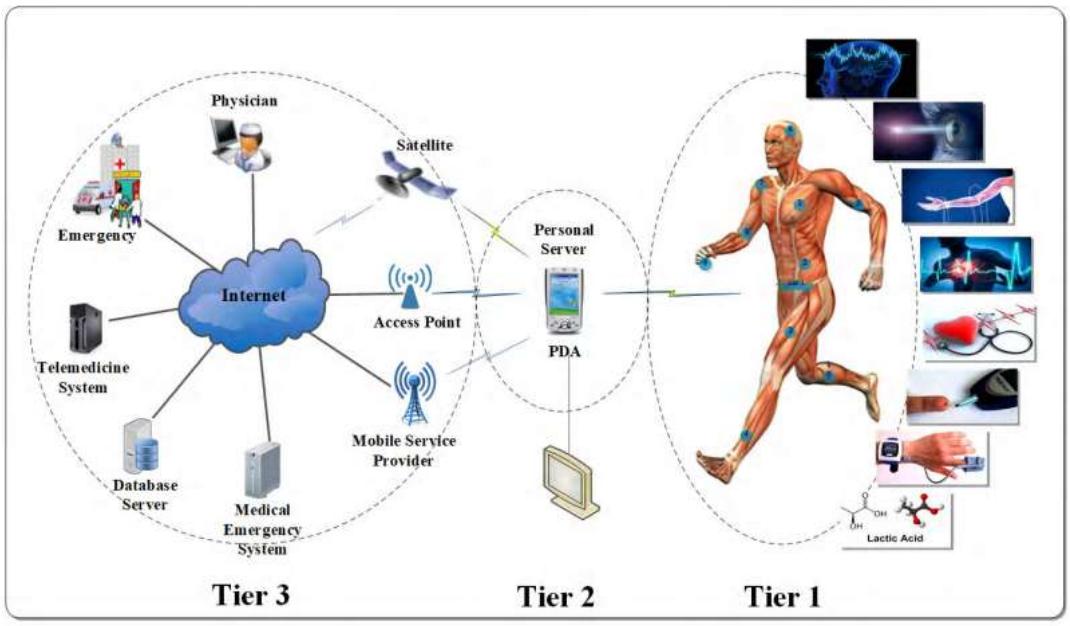

Figure 1.1. An example of a WBAN system application demonstrating a person wearing various health monitoring systems that transmit health data wirelessly to an on-body control unit, then over the internet by Ullah in "Robust and Efficient Energy Harvested-Aware Routing Protocol With Clustering Approach in Body Area Networks" © [2019] IEEE.

There are many challenges related to implementing WBAN systems, which include wireless body area channel characterization, wearable antenna design, and data privacy. A practical WBAN system should incorporate miniaturized sensors with long battery life. Body-worn sensors must be small so as to not interfere with the user's daily life. Additionally, the sensors in the WBAN system should have a long battery life, which improves the user's experience by not requiring constant charging. It would also reduce the risk of losing large periods of data that could be used for preventative medical care. Understanding the wireless body area propagation mechnism is important in order to achieving a practical WBAN system because the human body is a lossy medium that significantly affects antenna performance. There are three main EM wave propagation mechanisms, which are line-of-sight, wave scattering, and the creeping wave, which can

be seen in Figure 1.2. These mechanisms are affected by static and dynamic human bodies in different ways.

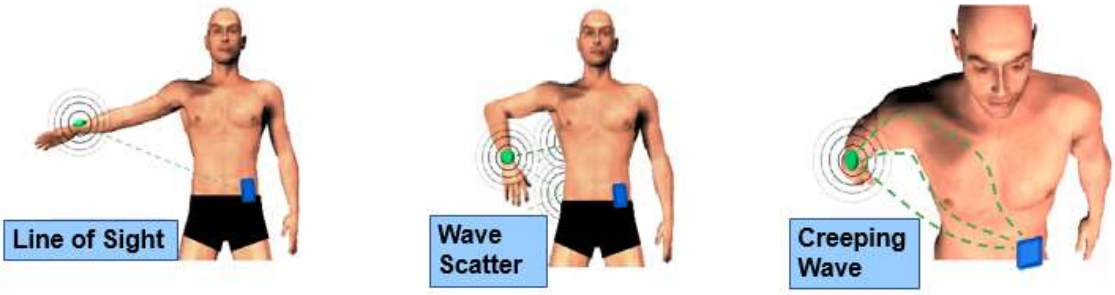

Figure 1.2. The three main on-body wave propagation mechanisms (left to right): line of sight, wave scatter, and creeping wave.

Practical WBAN design requires optimized on-body antenna design for these body-worn sensors. To avoid impeding the end user's daily life, such as with large sized sensors or needing constant re-charge, there must be a thorough understanding of on-body electromagnetic (EM) wave propagation and how the presence and motion of the human body can affect transmission between on-body devices. On-body antenna can be optimized to be smaller in size and efficient in power consumption. Smaller, power-efficient antenna will contribute greatly to allowing on-body sensors in WBAN systems to have practical, real-world usage. Creating an antenna that has a wearable profile for on-body scenarios is another challenge. There is a wide array of possible antenna types that can be used on the human body, ranging from monopoles to e-textile; however, each antenna type has limitations either in size, effect on daily activities when worn, or on-body performance. For example, previous works have found monopole antennas to have good on-body antenna performance [7]-[8], but the profile of a monopole antenna makes

wearing one for extended periods of time cumbersome. A balance between antenna profile and performance must be found.

Data privacy in WBAN systems is an important concern [9]-[11]. Many WBAN applications, such as in the medical field of military, would require the transfer of personal and private data between on-body devices and over the internet. Personal health data is confidential data and WBAN systems must be designed to prevent data from being intercepted while transmitted, such as using encryption, and the health data being transmitted needs an authentication method [11]. Restricting data access to ensure confidentiality is also a WBAN security issue [9]. WBAN systems must be developed with security measures in place to protect any confidential data from being leaked.

On-body EM wave propagation and antenna radiation are critical factors for implementing WBAN systems where the wave propagation mechanisms, such as the creeping wave, need to be accounted for when designing on-body sensors in order for optimal data transmission and reduced power draw. The human body can significantly affect EM wave propagation, which means the body will affect the antenna signal transmission between on-body devices, resulting in a need to design antenna that take advantage of wireless channel characterization for on-body scenarios. All of these mechanisms are impacted by the human body, which static body studies have shown.

There are even further human body effects on wave propagation mechanisms when the body is in motion. The optimal creeping wave pathway changes as antenna move to different positions on the human body [12]. Additionally, activities of daily motion can significantly affect antenna transmission strength [13]-[23]. Understanding the optimal on-body EM pathways can guide the design of antenna that will take

advantage of the naturally stronger EM pathways to reduce the human body effect on signal transmission. This can also result in reduced power consumption, resulting in optimal on-body antenna for WBAN applications. The ability to optimize antenna based on EM propagation mechanisms is why this research is necessary.

Literature Review

The potential of WBAN systems has led to many studies that sought to address the challenges associated with WBAN implementation, especially on-body channel characterization. Previous studies have been performed in the field of on-body wave propagation. These studies generally fall into measurement [13]-[22], simulation [21]-[27], and theory studies [28]-[32]. Various types of human body models have been studied as well, such as simplified cylinder-based models [23],[34], phantom models [17]-[20], Poser models [7]-[8], and 3D body scans of actual humans [21].

Previous works have studied on-body wave propagation using human and phantom model measurement techniques. Human measurement has many advantages, such as direct measurement of on-body antenna performance, not requiring computational resources, and often requiring less time to perform than computer simulations. Measurement of static human bodies has been performed by [7]-[8],[12],[33]. Static human measurement has revealed valuable information, such as which antenna types perform better on static human bodies [7] and the human body creeping wave effect [12],[33]. Figure 1.3 shows the measurement study used by [33] to study the creeping wave around the human body by moving two antennas around a human volunteer's torso. Human motion does have a significant impact on on-body antenna transmission, which means dynamic measurement must also be considered.

Many dynamic measurement studies have used human volunteers to measure on-body signal data in various environments [13] and for various activities of daily living, such as walking, running, falling, and cycling [13]-[22]. An example of cycling from [15] is shown in Figure 1.4. However, these studies have limitations by virtue of dependence on physical measurement. Measurement based studies can only record antenna transmission data at the points where antennas are worn, and can be time consuming, especially for the human volunteers involved in the data collection process. Additionally, these measurement based studies often do not record human body motion, which reduces the ability to correlate antenna performance with body position or motion [14]-[16],[18]-[20]. Additionally, utilization of motion capture techniques, such as 3-D body scanning, has generated realistic human body models, but has not always resulted in high resolution capture of body motion due to low frame rate motion capture [21].

Figure 1.3. A static on-body measurement setup used to study the creeping wave effect used by Xue in "Simulation and measurement of on-body wave propagations" © [2014] IEEE.

Some previous works have utilized phantom models in measurement. Phantom models have been used to study human body effects in both static and dynamic body

scenarios [17]-[20] and phantom models have been used to assess antenna performance [19]-[20]. Applications range from off-body antenna effects for static phantom models [17] to on-body antenna effects for dynamic phantom models [18]-[20]. The measurement phantom used by [18]-[20] which has arm swinging capabilities can be seen in Figure 1.5. The phantom model was used to study on-body fading effects by using an arm swinging motion. The model's accuracy was compared to one human volunteer using voltage standing wave ratio (VSWR), gain, and path loss for arm swinging motions at 915MHz, with some limitations due to the single frequency analysis and single volunteer used for phantom validation.

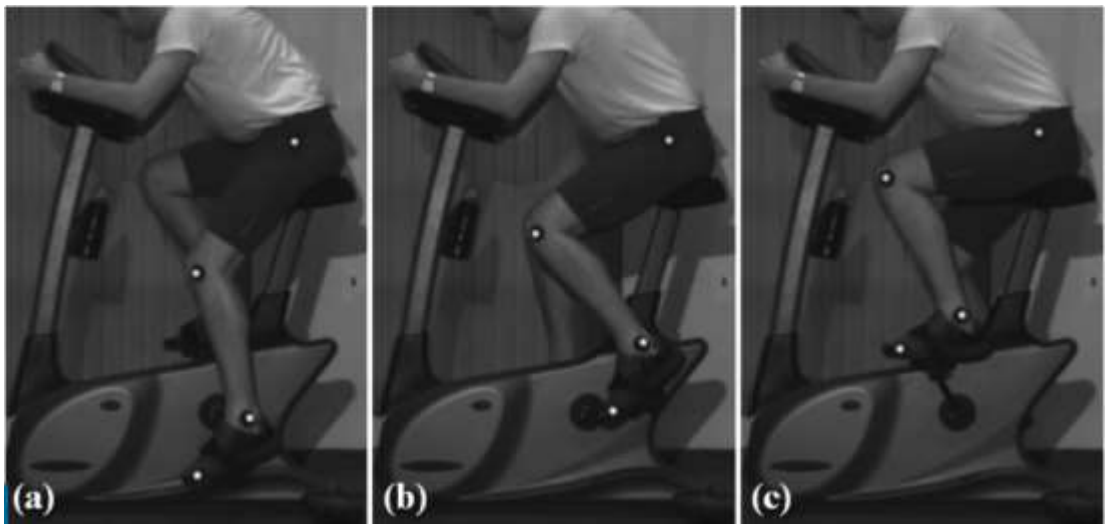

Figure 1.4. An example of human cycling motions from Munoz in "Exploring Physiological Parameters in Dynamic WBAN Channels" © [2014] IEEE.

Figure 1.5. The arm swinging human body phantom model used by Yamamoto in "BAN Radio Link Characterization Using an Arm-Swinging Dynamic Phantom Replicating Human Walking Motion." © [2013] IEEE.

Simulation studies can alleviate some of the limitations of measurement, such as having the ability to simulate entire EM pathways between the on-body antennas. Additionally, antenna positions and body parameters can be easily changed in simulation. Previous works have used computer simulation techniques to study on-body wave propagation [21]-[27]. Many human body simulation models have been evaluated, ranging from simplified cylindrical models [23]-[25],[27], realistic Poser models [23]-[25], voxel models [26], and 3D body scanned models [21]. A comparison of simplified cylindrical model and the more realistic Poser model simulation setup from [23] can be seen in Figure 1.6. Some studies performed comparison of simulation with measurement and achieved good agreement, but many did not correlate body position with antenna performance, which often resulted in human volunteers mimicking the simulation model's motions, which resulted in a comparison that would not completely capture the

same body motion effects on wave propagation. Figure 1.7 shows Poser simulation and simplified simulation models used to compare with human measurement from [25]. These studies used many types of simulation models and were able to get generally good agreement between measurement and simulation, which supports the results from [23], which found similar performance between cylindrical and Poser models.

Simulation work has been performed to determine the differences between homogeneous and heterogeneous human body models [24],[26]. For on-body applications, homogeneous tissue properties, such as muscle or skin, have been shown to provide accurate simulation results when compared to human measurement [24-[25]. Our previous work [34] has utilized high frame rate motion capture to allow for body position to be used in simulation and compared with human measurement. Frame-by-frame CST simulation based on motion capture models from [34] can be seen in Figure 1.8. Simulation does have some disadvantages, which include computational time, not including environmental effects that would appear in measurement, modelling different body types, and matching exact dielectric properties with actual humans.

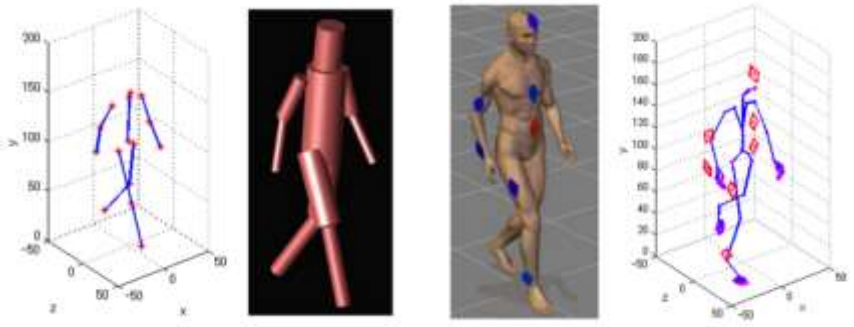

Figure 1.6. Cylindrical and Poser simulation models used by Iswandi in "The Utilization of Body Skeleton Model for Modeling the Dynamic BAN Channels" © [2012] IEEE.

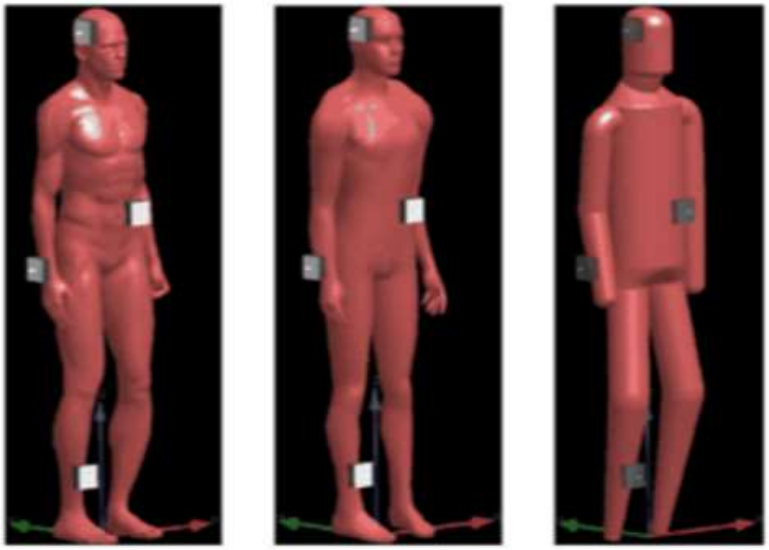

Figure 1.7. Simplified and Poser simulation models used by Gallo in "Simulation and Measurement of Dynamic On-Body Communication Channels" © [2011] IEEE.

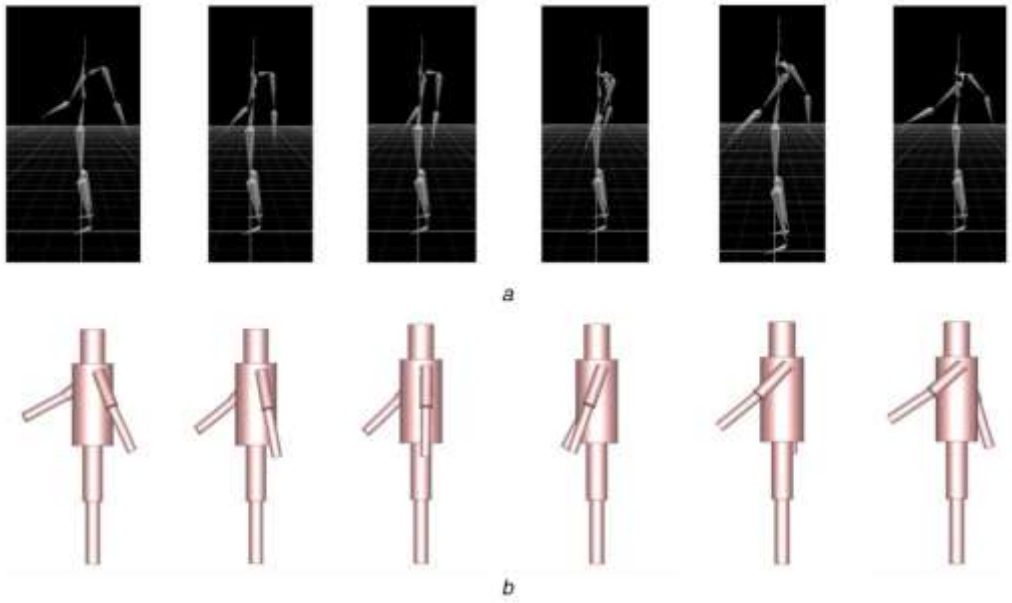

Figure 1.8. (Top) Motion capture skeletons with (bottom) the corresponding CST cylindrical simulation models positioned based on the skeleton motion data by Lee in "Simulation and measurement of electromagnetic wave propagation on dynamic human bodies" © [2017] IET.

Additionally, theoretical work has been done to evaluate on-body EM wave propagation [28]-[32]. Theory-based studies derive field solutions for various WBAN

scenarios. Some static studies use homogeneous mediums of varying shapes, such as cylinders or slabs [28]-[29]. Additional work has been done to evaluate heterogeneous bodies due to the lossy nature of human body tissue [30]. The use of theoretical models to study heterogeneous body models is advantageous as assembling heterogeneous body models can be costly. Often, theory models are compared to simulation for verification [28]-[29]. Additional analysis has been done through comparison with human measurement as well [28]. A portion of the analytical derivation of the on-body E-field from [28] can be seen in Figure 1.9. Theoretical work has also been performed to assess the performance of wireless optical communication for WBAN by using probability and evaluating blocking of optical beams by the human body [31]. Dynamic studies have compared analytical models with human measurement with good agreement [32].

These theoretical models have similar results when compared to other methods of EM analysis, such as measurement and simulation [28]-[29],[32]. Figure 1.10 shows a comparison of analytical and simulation models from [32], demonstrating the analytical models generate similar results to finite-difference time-domain (FDTD) simulation. Theoretical models are also capability of being used to study EM wave propagation mechanisms, such as the creeping wave [32]. Theoretical analysis of EM field solutions provides valuable insight into body effects on EM wave propagation; however, these studies are often limited to static body cases.

$$E_r = -\frac{jk_0 aIdlZ_0}{4\pi b}\frac{\exp(-jk_0 a\theta)}{d}e^{j(\omega_0-\pi/4)}2(\pi x)^{1/2}\times$$
$$\sum_{s=1}^{\infty}\frac{e^{-jxt_s}}{t_s-q^2}\frac{w_1(t_s-y_1)}{w_1(t_s)}\frac{w_1(t_s-y_2)}{w_1(t_s)}$$
$$-\frac{jk_0 aIdlZ_0}{4\pi b}\frac{\exp(-jk_0 a\theta_c)}{d}e^{j(\omega_0-\pi/4)}2(\pi x_c)^{1/2}\times$$
$$\sum_{s=1}^{\infty}\frac{e^{-jxt_s}}{t_s-q^2}\frac{w_1(t_s-y_1)}{w_1(t_s)}\frac{w_1(t_s-y_2)}{w_1(t_s)}$$

Figure 1.9. Equations for E-field calculation used by Conway in "An Analytical Path-Loss Model for On-Body Radio Propagation" © [2010] IEEE.

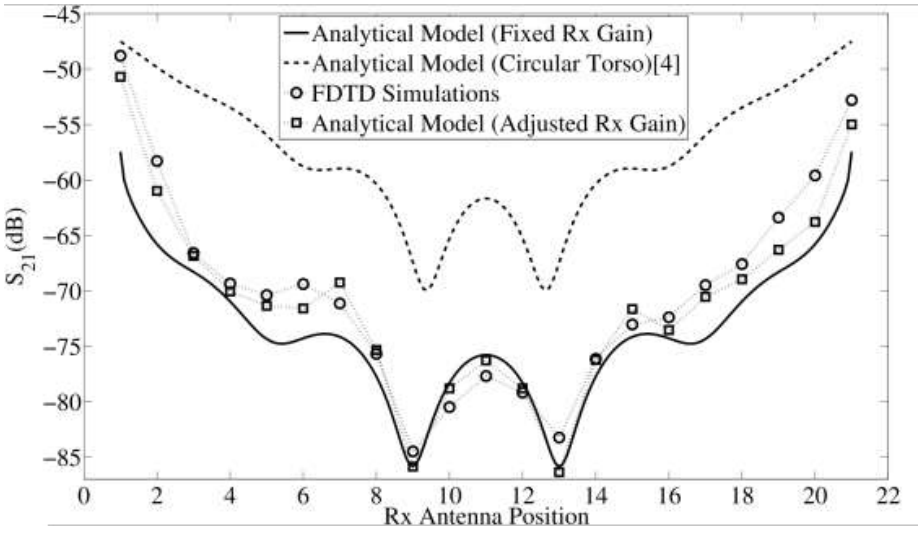

Figure 1.10. Comparison of S_{21} and antenna position for analytical and simulation models by Chandra in "An elliptical analytical loss model for wireless propagation around the human torso" © [2012] IEEE

Study Objectives

This dissertation seeks to combine measurement and simulation techniques in order to study on-body wave propagation using a human body phantom model. The phantom model has the potential to serve as a robust framework that can be used to assess on-body EM propagation pathways, serve as a simulation model for on-body antenna

design, and as a measurement validation tool for testing fabricated on-body antennas. The phantom model approach has many benefits, such as a more controlled measurement environment, a modular design, and fewer time constraints than using human volunteers for measurement. A controlled environment for measurement will allow for measurement test procedures to be more repeatable and for specific parameters to be changed independently. The phantom model will be modular in design, which will allow for different body parameters to be tested. The phantom model is also more readily replicated in computer simulation than a human body, allowing for more complete simulation model verification.

In addition, this dissertation will improve on previous phantom study limitations by using motion capture to track the phantom's motion and more comparison with human measurement data at various frequencies. Motion capture will be used in simulation to accurately move the simulation model to match measurement. Additionally, motion capture data will be used to gain greater insight into motion effects on antenna signal strength by using body angles for analysis. As stated before, previous studies have performed simulations or developed types of phantom models, but our use of high resolution motion capture to analyze body effects on antenna signal transmission and to provide direct simulation comparison will provide greater insight into on-body wave propagation than previous studies.

After the phantom model has been developed, it will be validated using both measurement and simulation techniques. The phantom model will have motion capture data and antenna transmission data measured while it performs controlled arm-swinging motions. Human volunteers will be used for comparison, who will also perform arm-

swinging motions in a matching configuration of antenna, antenna placement, and motion speed. Using the motion capture data from the phantom measurement, a phantom simulation model will be developed. The simulation model will be controlled by an in-house macro in CST, a 3D EM simulation software, that uses motion capture data to move the arm position, which allows for direct comparison of measurement and simulation. The phantom measurement, human measurement, and phantom simulation will be compared in order to validate the effectiveness of the phantom model as a platform for further study of on-body EM wave propagation. Previous studies, such as [21] and [25] have compared differences in S_{21} for human measurement and computer models and a similar comparison is performed in this study.

Following the validation of the phantom model, a parametric study will be performed. This study will evaluate the human body and motion factors that affect on-body wave propagation. This parametric study will focus on antenna frequency, antenna placement, and phantom dielectric properties. The key frequencies are 433MHz, 915MHz, and 2.45GHz, which are in the ISM band [37], which is used for medical applications. The antenna placements represent potential placements of real-world on-body sensors, which will make analysis of antenna transmission strength relevant. Dielectric properties of the phantom model are modified to see how the presence of the human body affects EM wave propagation. The modular nature of the phantom model will allow for this study to be performed, where antenna frequency, placement, and phantom dielectric properties can be easily modified.

The final part of this dissertation will study the performance of different antenna types on the phantom model. Different antenna types have different form factors and

propagation patterns, which can affect usability and on-body performance, which makes antenna type critical to designing on-body antenna. The antenna types investigated are the monopole antenna, microstrip patch antenna, and e-textile antenna. These antennas have very different form factors, which makes this comparison of performance interesting because a real-world on-body antenna should have the most unobtrusive form factor possible, such as being imbedded into clothing, while retaining usable antenna performance.

In summary, this dissertation will use a human body phantom model approach to gain further insight into on-body EM wave propagation by accomplishing the following four goals:

(1) Developing an arm-swinging human body phantom model (Chapter Two)

(2) Validating the human body phantom model through measurement and simulation (Chapter Three)

(3) Performing a parametric study using the human body phantom model (Chapter Four)

(4) Evaluating various wearable antenna designs using the human body phantom model (Chapter Five)

CHAPTER TWO

Development of an Arm-Swinging Phantom Model

Phantom Model Properties

A phantom model for use in the study of on-body EM wave propagation must be capable of controllable motion, and be modular in design, which lead to significant advantages in measurement when compared to human volunteers. Controllable motion allows for more repeatable and consistent results due to motion speed and range being well defined. Human volunteers, even with direction and a metronome can have more variations in motion speed or motion pattern than a phantom model. The main parameters that must be modular are the phantom's dielectric properties and phantom body size. The ability to modify dielectric properties can help expose possible effects of different body types, such as those with different amounts of body fat or muscle, or to isolate the effect of motion from the body effect. Phantom body size modularity allows for the capability to test the effect of body shape and size on on-body wave propagation. These factors combined give the phantom the capability to be used in studies that can cover wide variations in body type.

The phantom model is designed to be made of multiple hollow plexiglass segments that consist of a torso, arms, and head. The arms are connected to the torso using wooden rods, which are turned and controlled by our motor control system. The assembled phantom model can be seen in Figure 2.1. The arm swing speed is controlled using a motor control system consisting of a stepper motor, stepper motor driver, and Arduino UNO, which turn the arms of the phantom. The motor control system can be

seen in Figure 2.2. The Arduino clock speed is programmed to provide a smooth swing pattern for the arm by using a stepping speed that is not constant throughout the arm swing motion. The motor control system can vary the length of time and speed ranges during the programmed arm swing patter. Thus, the control system can be programmed with different arm swing speeds and arm swing ranges, providing consistent arm swinging motions. The arms can be programmed to achieve similar motion speeds and ranges as human volunteers, allowing for fair comparison between phantom and human measurement for verification. It should be noted that the phantom range of motion will be similar to the range of motion of the human volunteers, but will not be an exact match due to the variable nature of human motion, where there are noticeable differences in motion range between arm swings and between different human volunteers. Plexiglass and wood were chosen due to their minimal effect on EM wave propagation. The hollow design allows for the phantom to be filled with various tissue simulating solutions, allowing for modular dielectric constant. The segments can be different sizes, giving the phantom modular size capability.

The phantom model was constructed using 0.635cm thick plexiglass sheet and plexiglass tubing. The sizes of the body sections of the phantom model can be seen in Table 2.1. The torso was shaped using a mold for heated plexiglass sheet to be formed onto. The tops and bottoms of the segments of the phantom body were sealed using a plastic cement (Weld-On 16) designed for use with plexiglass. The torso was designed to have a hollow through-hole that holds mounting rods that hold the phantom model's arms. The arms similarly have through-holes that allow for the mount rod to pass through, which have mounting points that allow the arm to be secured on the rod using

nylon bolts. The mounting rods connect to the previously mentioned motor control system, which allows the arms to be rotated along with the mounting rods. The hollow phantom model design was sealed with silicone to be capable of holding the muscle tissue simulating solution without leaking. A stress analysis based on the size of the hollow shell, the tensile strength of the plexiglass, and the weight of the liquid that the plexiglass body sections, showed the pressure from the muscle tissue simulating solution would not cause the plexiglass shell to fail.

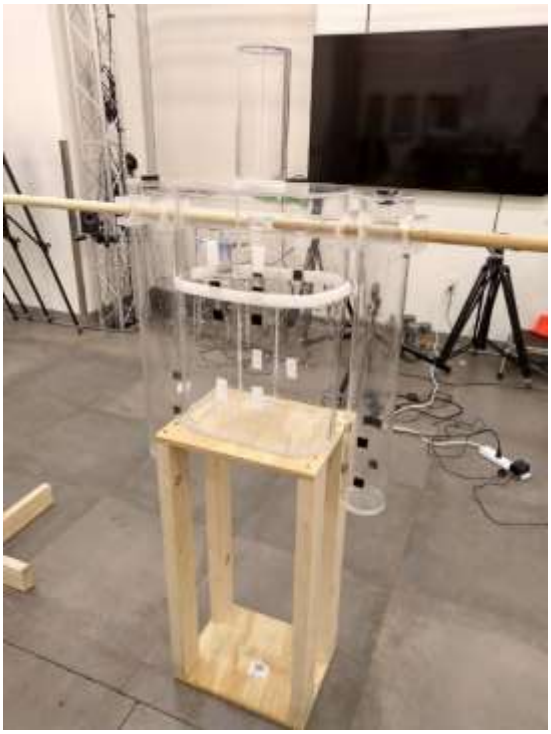

Figure 2.1. The human body phantom model placed on a wooden stand with arms attached by the wooden arm rotation control rods.

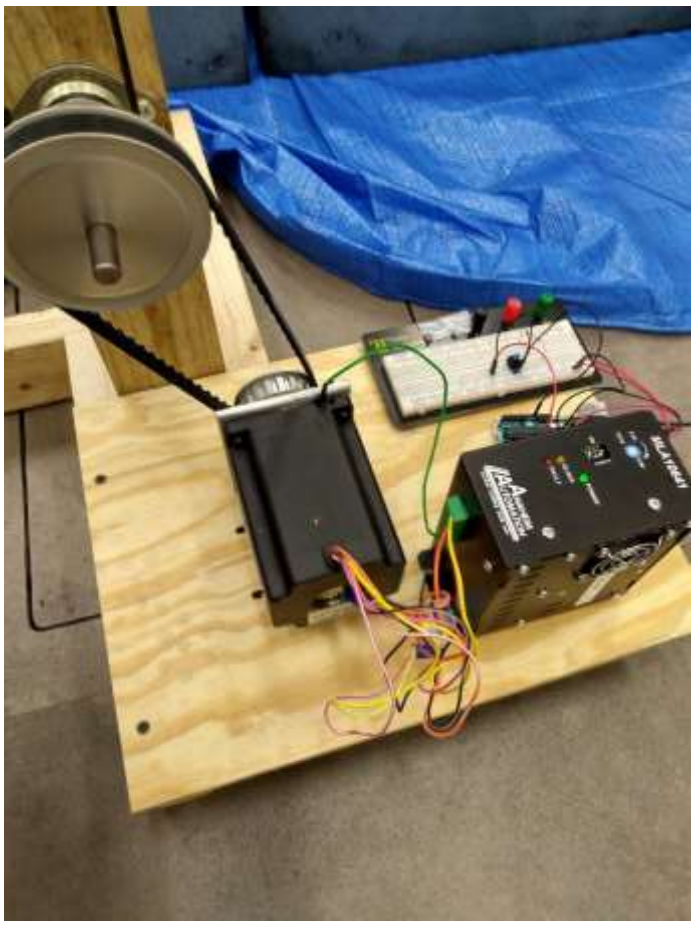

Figure 2.2. The motor control system which consist of (left to right): a belt and pulley system, stepper motor, and stepper motor driver.

Table 2.1. Human body phantom model dimensions.

Body Part	Length (cm)	Circumference (cm)
Torso	53.7	102.9
Arm	68.6	33

The tissue simulating solution can be mixed using distilled water, sugar, and salt. The solution used in this study is 53.0% distilled water, 45.8% sugar, and 1.2% salt, based on values from [35]. The solution is capable of having varied dielectric properties by varying the percentage of water, sugar, and salt used. The muscle tissue simulating solution being mixed can be seen in Figure 2.3, and the phantom in Figure 8 is also

shown filled with muscle tissue simulation solution. This can result in different tissue properties, such as skin or muscle tissue. Previous studies, such as those by Hall and Gallo, have already shown that homogeneous body tissue properties, such as muscle, are effective at modeling the human body in simulation for on-body antenna cases. This is the basis for our measurement techniques that utilize a phantom model with homogeneous dielectric properties using plexiglass, which is essentially electrically invisible, filled with a homogeneous muscle tissue simulating solution. The muscle tissue simulation solution is based on human muscle and is verified through measurement using a dielectric probe. The measurement of the muscle tissue simulation solution's dielectric properties can be seen in Figure 2.4. The dielectric properties of the muscle tissue simulating solution can be seen in Table 2.2, with theoretical values from [36]. The dielectric properties of the phantom model are similar to the theoretical dielectric properties of muscle, showing the phantom can replicate human muscle tissue properties. The phantom model can potentially be used for in-body antenna studies if additional compartments are added into the body segments, which could emulate organs and other body tissues that don't necessarily match the dielectric properties of muscle and skin, which are the tissue properties most used in previous on-body studies. This expansion of the model is potential future work for the phantom model that will not be covered in this dissertation, but shows the value the phantom model can provide.

The muscle tissue mimicking solution is also able to be used for long periods of time without significant changes in the dielectric properties. Figure 2.5 shows the change in permittivity in the solution over five days at 433MHz, 915MHz, and 2.45GHz. The permittivity does not change more than six at each frequency, which is not a significant

change. Figure 2.6 shows the change in conductivity over five days at 433MHz, 915MHz, and 2.45GHz. The conductivity doesn't change more than 0.5 S/m over five days, which is not a significant change in conductivity.

Table 2.2. Dielectric properties of muscle tissue simulation solution compared to theoretical muscle tissue at 915MHz.

Dielectric Property	Muscle Tissue Simulation Solution	Theoretical Muscle
Permittivity	54.45	55.92
Conductivity (S/m)	1.14	0.97

Figure 2.3. A sample of the muscle tissue simulation solution being mixed.

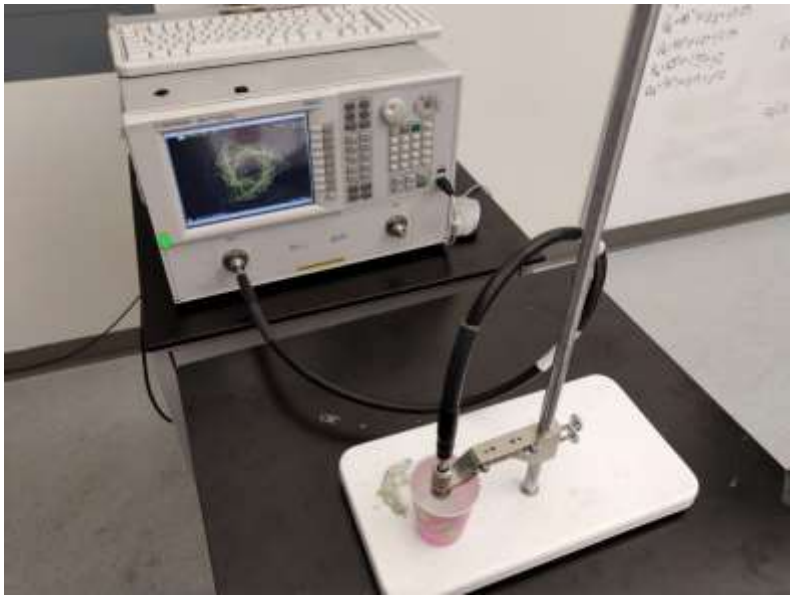

Figure 2.4. Dielectric property measurement setup utilizing a VNA (top) and dielectric probe (bottom).

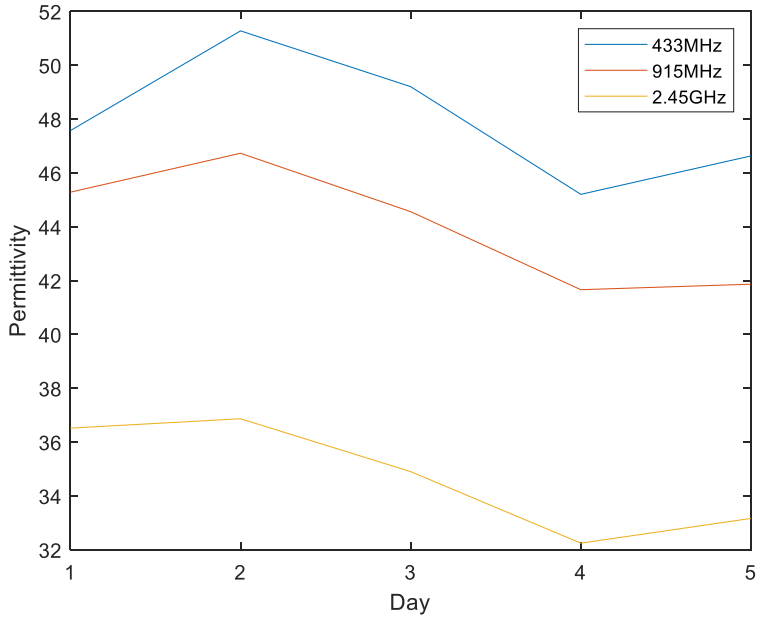

Figure 2.5. Permittivity of the muscle tissue mimicking solution over five days at 433MHz, 915MHz, and 2.45GHz.

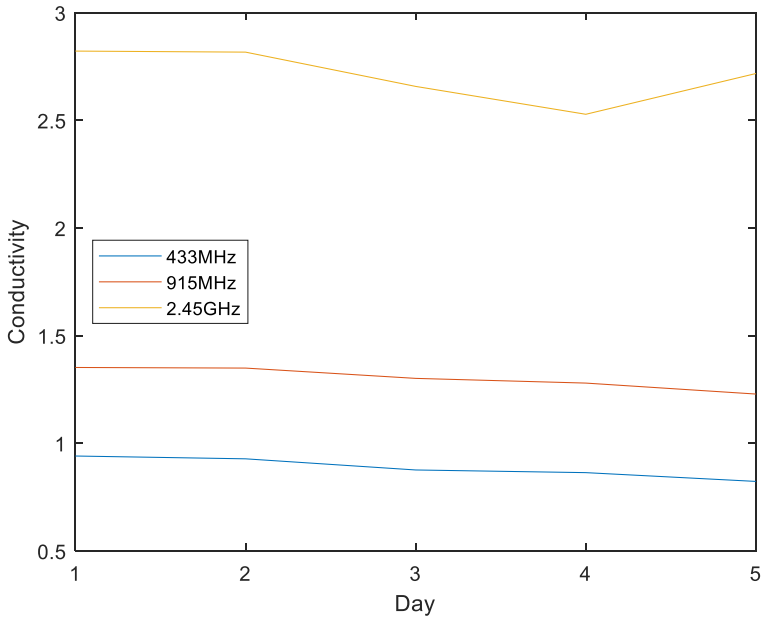

Figure 2.6. Conductivity of the muscle tissue mimicking solution over five days at 433MHz, 915MHz, and 2.45GHz.

Measurement Techniques

The measurement technique utilizes a combination of motion capture techniques and a vector network analyzer (VNA). The use of motion capture is critical for analysis of motion effects on antenna signal strength. The motion capture data is also fed into our in-house macro for CST, a 3D EM simulation software, which uses the data to control the phantom model's motion in simulation, which will be discussed in further detail below. Two types of motion capture system are used: a Phasespace active marker system and a Vicon passive marker system. The two systems differ in their motion capture marker systems, where the active system consists of a bodysuit with LED markers and the passive system consists of reflective markers that can be placed on the body itself. The Vicon passive system was used for marker placement on the phantom model for tracking of the phantom's arm motion. The Phasespace active system was used with the human

volunteers, with the antenna having points for consistent attachment on the bodysuit using Velcro. Both of the motion capture systems are time synchronized with the VNA, allowing for the motion and antenna signal data to be compared in time, and thus allowing for motion effects on EM wave propagation to be analyzed by comparing motion data with the antenna signal data. The Vicon motion capture setup for the phantom can be seen in Figure 2.7 and the Phasespace motion capture setup for human volunteers can be seen in Figure 2.8.

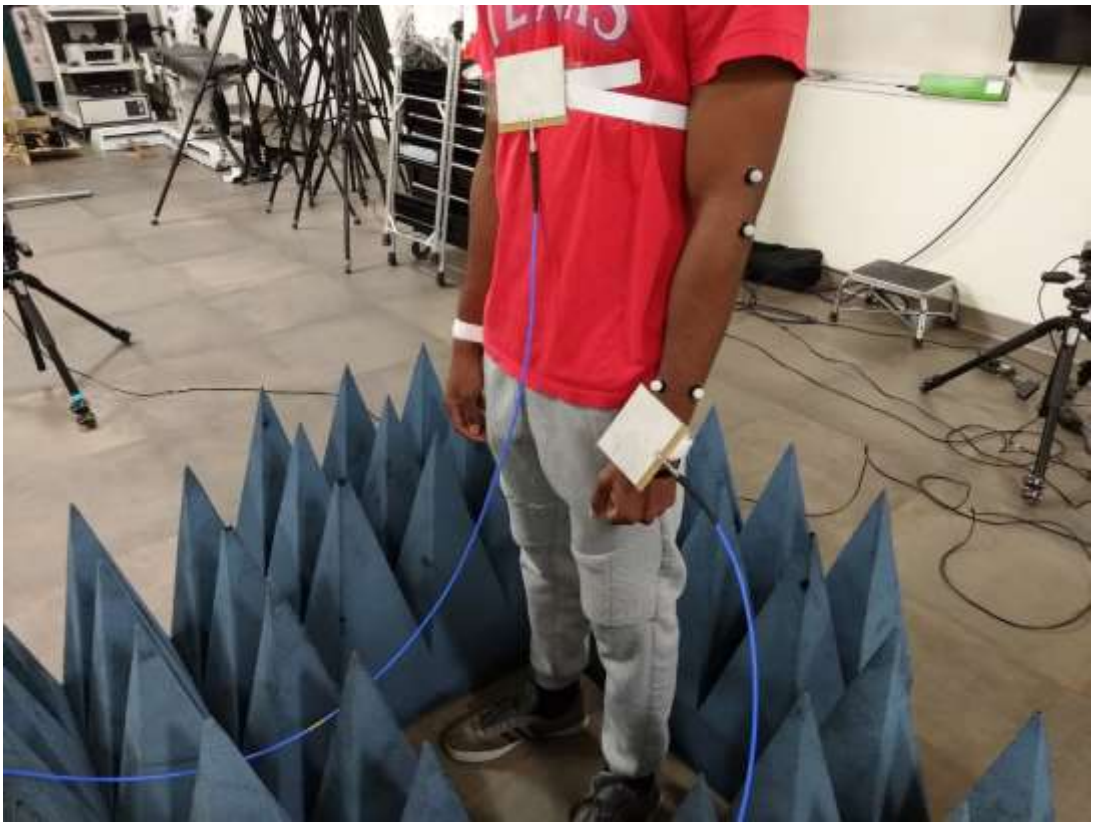

Figure 2.7. A human volunteer standing in a Vicon motion capture camera capture space, surrounded by ground absorbers, and wearing microstrip antennas on the chest and front of the left wrist with passive motion capture markers placed along the left arm.

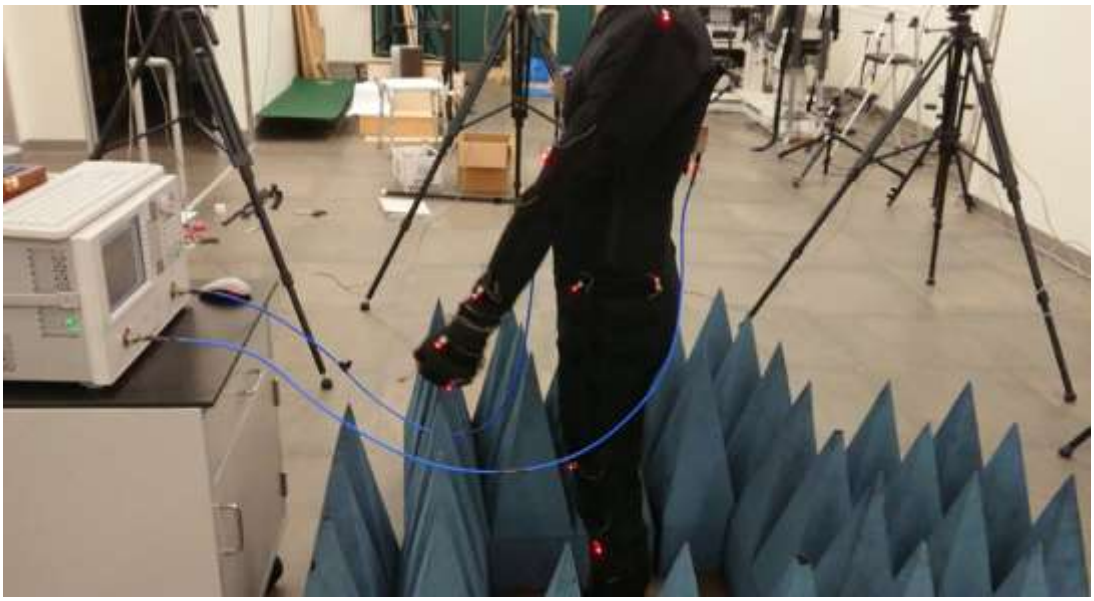

Figure 2.8. A human volunteer standing in a Phasespace motion capture camera capture space, surrounded by ground absorbers, and wearing monopole antennas on the chest and back and an active marker motion capture suit.

Passive motion capture markers were placed along the arm of the phantom model. The markers were placed in-line along the phantom's arm. This configuration was chosen because it would allow for the arm angle during the arm swing motion to be calculated simply. Three lines of markers were placed along the phantom model's arm in order to ensure enough markers would be seen in order for the arm angle to calculated in case of potential motion capture marker occlusion.

Human volunteers wore a Phasespace motion capture suit that features active LED motion capture markers along the entire body. The markers along the arm were used to calculate the arm swing angle of the human volunteers, allowing for an arm swing comparison with the phantom model. The motion capture cameras were placed such that marker occlusion was minimized, especially for the markers on the arms.

Simulation Techniques

The phantom model was re-created in CST, a 3D EM simulation software, in order to perform computer simulations of the antenna signal strength during the phantom's motion. The dimensions of the constructed phantom model were used to define the phantom's size in CST. The dielectric properties of the plexiglass and muscle tissue simulating fluid were measured using a dielectric probe. These measured dielectric properties were used to define the dielectric properties of the phantom model in CST.

An in-house CST macro was developed to allow for the simulation of an entire range of motion over time. The VBA macro is used to control CST to perform multiple simulations of consecutive frames of time. This emulates the motion of the actual phantom using CST. The simulations are performed using CST's time domain solver. The arm angles of the phantom model are calculated using the motion capture markers placed on the phantom model's arm. The motion capture data produces 3D position data for the motion capture markers, which provide X, Y, and Z directional distance from the motion capture space's origin position. Using the Phasespace motion capture software allows the motion capture data to be converted into a motion capture skeleton model of the human body when the appropriate full-body motion capture marker set it used. The motion capture model skeletons from Phasespace can be seen in Figure 2.9. The skeleton represents the key segments of the human body, such as the torso or arms. Knowing which markers are used to define the sections of the body skeleton allows for the arm swing angle to be calculated using the marker coordinate data using the arctangent of the shoulder and arm markers. This method of calculating arm angles can be used for the Vicon marker coordinate data as well. The arm angles for the motion capture are

organized into a text file that the macro can read. The arm angles provide the macro with the proper rotation for the appropriate arm, which allows the phantom arm to be in the correct position for the current frame of time. The simulations are performed at 10 frames per second due to the significant simulation times at higher frequencies, such as 915MHz. However, the simulations can be performed at up to 120 frames per second, which is the capture rate of the motion capture system. A few sample frames of the frame-by-frame simulation setup used to simulate the phantom model's entire range of motion can be seen in Figure 2.10.

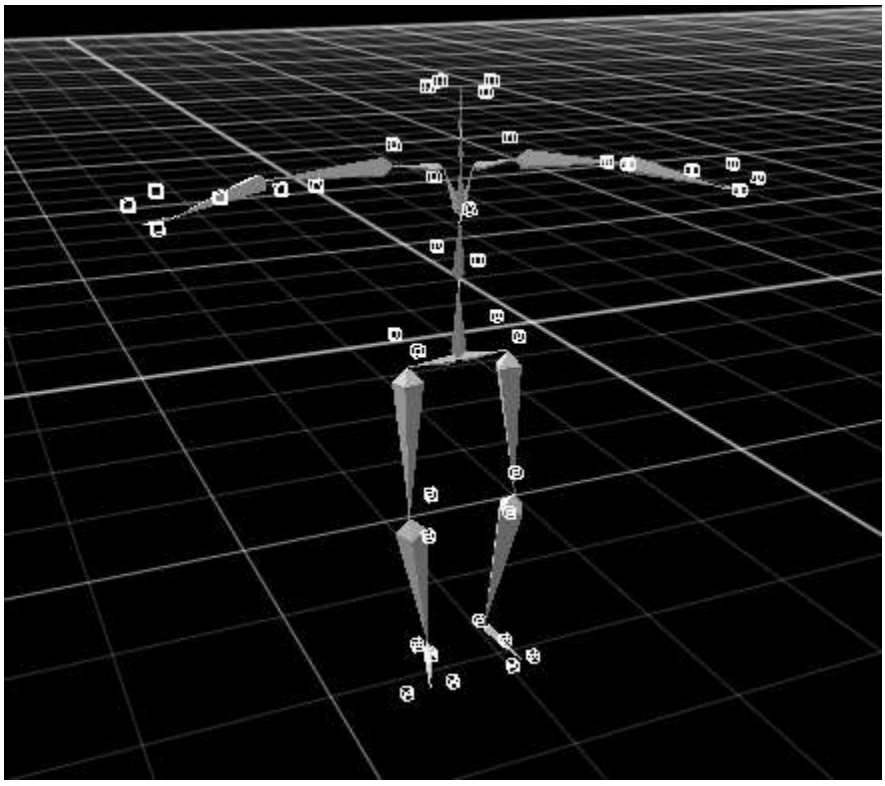

Figure 2.9. A human body skeleton model created using Phasespace Recap2 software based on motion capture marker data.

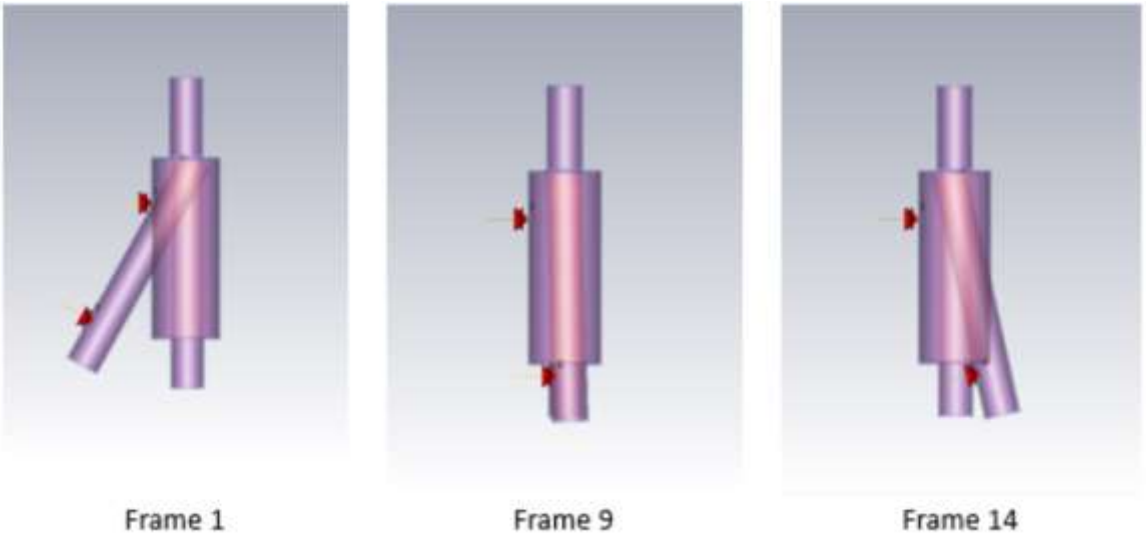

Figure 2.10. A few sample frames of the frame-by-frame simulation technique this study uses in CST to simulate entire ranges of motion, such as the arm swing motion shown.

Summary

A phantom model approach has many advantages for studying on-body EM wave propagation, such as motion consistency and the ability to easily change various body parameters with a modular phantom design. A plexiglass human torso phantom model was constructed and a muscle tissue simulating solution was developed for use at 433MHz, 915MHz, and 2.45GHz. A measurement setup that incorporates time synchronized motion capture and vector network analyzer was used for data collection. A frame-by frame CST simulation macro capable of using motion capture data for model motion was developed for the phantom model.

CHAPTER THREE

Phantom Model Validation Using Monopole Antennas

The first test of the phantom model was measurement using bridge monopole antennas. The operating frequency of the monopole antennas was 915MHz. The antennas used in this study consisted of a steel ground plane and copper wire. The dimensions of the ground plane were 11.43cm long by 3.81cm width, with a height of 1.27cm in the center third of the ground plane. The length of the copper wire was 8.2cm for 915MHz. The antennas used can be seen in Figure 3.1. The monopole antenna resonance was tested on the human body to ensure that the antennas had proper resonance during on-body usage. Figure 3.2 shows the reflection coefficient, S_{11}, vs frequency. Reflection coefficient can be used to measure whether an antenna is resonating at a certain frequency, where an S_{11} below -10dB indicates the antenna resonates at the corresponding operating frequency. The results show that the antenna does resonate at 915MHz due to the S_{11} dropping below -10dB at 915MHz. This verifies that the antennas being used were resonating at our desired frequency while being used in an on-body scenario, which enabled us to use the antenna for our dynamic on-body study.

The phantom model has many useful measurement capabilities, which have been mentioned above; however, the phantom must be verified using comparison with human measurement data. Additional verification was performed using CST simulation. Comparing phantom measurement with phantom simulation and human measurement can confirm whether the phantom model is able to accurately represent the human body for

on-body wave propagation measurement. The phantom model simulation had its arm motion controlled using motion capture data taken from the phantom measurement.

Figure 3.1. 915MHz monopole antenna consisting of a steel ground plane and copper wire with a coaxial connection.

The monopole antennas were placed on the chest and the front of the left wrist of the phantom model, now referred to as chest/left wrist (front), which can be seen in Figure 3.3. The phantom model performed arm swinging motions at a 3.0s cadence, with an arm swing range programmed to be similar to the arm swinging range of the human volunteers. The arm swing cadence refers to the time it takes for one cycle of arm swinging to complete. The cycle of an arm swing is defined as the arm starting at its most

forward position in front of the torso (most flexed at the shoulder), then moving backwards behind the body to its most extended position at the shoulder, and then moving back to the starting forward position. The phantom model was filled with muscle tissue simulating solution, with dielectric properties listed in Table 2. The comparison between the produced muscle tissue simulating solution and the theoretical dielectric properties of homogenous human muscle previously seen in Table 1 shows that the muscle tissue simulating solution has similar properties to actual muscle. In addition to previous works, such as [25], suggesting homogeneous models are effective for studying on-body wave propagation, the muscle tissue simulating solution can be used to represent human tissue properties in the phantom model.

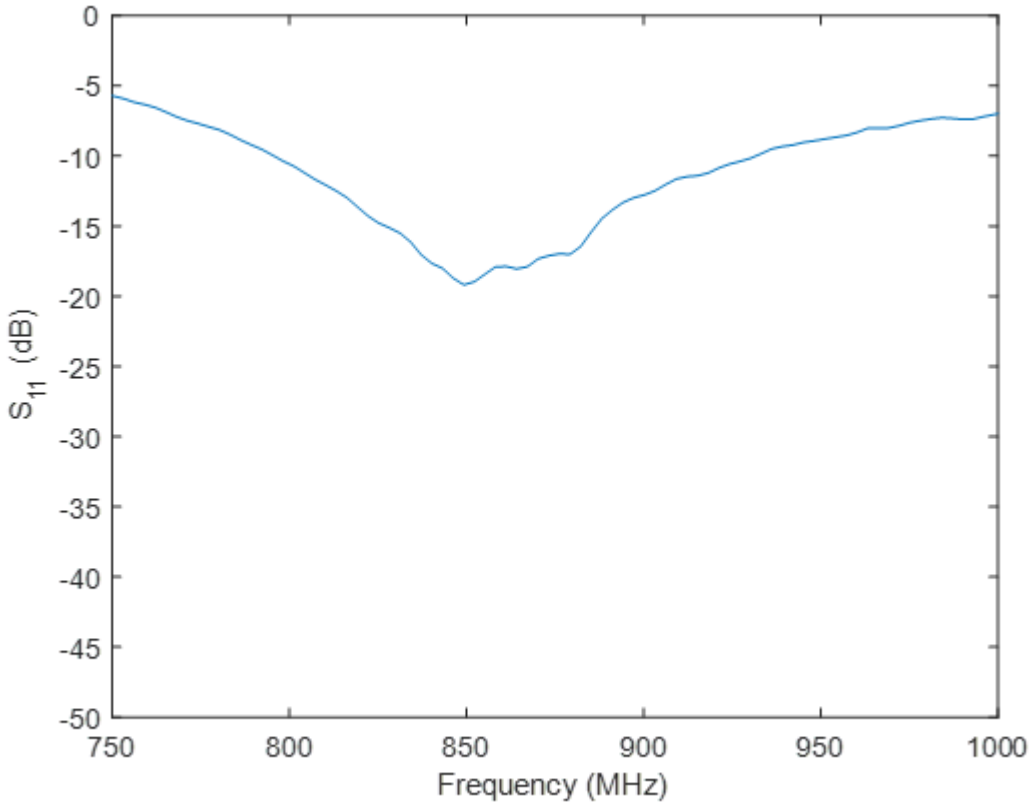

Figure 3.2. Reflection coefficient vs. frequency for a 915MHz monopole antenna worn on the chest of a human volunteer.

The measurement of the phantom model, the measurement of the human volunteer, and the simulation of the phantom model were compared to determine whether the phantom model has a similar effect on EM wave propagation during dynamic motion. The analysis was performed by comparing S_{21} vs time and S_{21} vs arm angle, where S_{21} is the transmission coefficient, which is a measure of how strong the signal between two antenna is, with higher S_{21} meaning greater signal strength. The similar cadence produced by the motor control system and the human volunteers following a metronome allows for similarities in S_{21} pattern and periodicity over time to be seen. The use of motion capture on both the phantom model and human volunteers allow for a comparison of how motion and body position affects S_{21}.

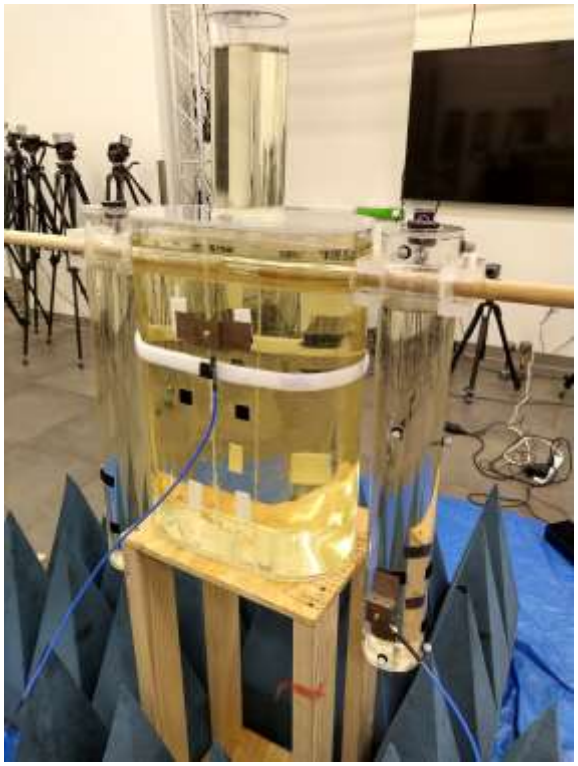

Figure 3.3. The human body phantom model filled with muscle tissue simulation solution wearing 915MHz monopole antennas in the chest/left wrist (front) configuration.

Before the S_{21} analysis can be performed, the antenna performance through S_{11} must be taken into account. Figure 3.4 shows S_{11} vs time for the 915MHz measurement of the phantom model wearing the monopole antennas in the chest/left wrist (front) antenna configuration. The S_{11} data is taken from the antenna placed on the phantom wrist. This S_{11} vs time data was recorded during the arm swing motion of the phantom model. The data serves two purposes, which are to verify the resonance of the antenna while placed on the phantom model's body and to see what effect the body motion may have on S_{11}. Figure 3.4 clearly shows that the S_{11} stays consistently below -10dB for the duration of the arm swing motion trial, which shows that the antenna is able to resonate at 915MHz while on a phantom body and during motion. It can also be seen that there is a fluctuation pattern in the S_{11}. The S_{11} has a repeating peak and dip pattern, characterized by S_{11} peaks approaching -15dB and dips below -18dB, with an M-shaped fluctuation during the dip periods, for example from 2.0s to 3.7s. This shows that the motion of the phantom arm does have a repeated periodic effect on S_{11}, which is reinforced by the 3.0s cadence of the S_{11} fluctuation pattern matching the 3.0s arm swing cadence used during measurement.

Figure 3.5 shows S_{21} vs time at 915MHz for the phantom model wearing the monopole antennas in the chest/left wrist (front) configuration. Based on the results in Figure 3.5 a peak to dip pattern can be seen in the S_{21} over time, which repeats with a predictable periodicity. This suggests the arm swinging motion does have an effect on the S_{21}, which is likely caused by both the motion of the antenna and the presence of the human body. The peaks and dips can be attributed to the arm swinging motion cycle. The signal drops as the arm swings behind the torso (0.8s to 1.4s), increases as the arm moves

forward in front of the torso (1.4s to 2.1s), then shows a slight M-shape while the arm stays in front of the torso (2.1s to 3.8s). The motion and body effect both affect the primary EM wave propagation mechanisms, as motion changes the position between antennas and changes the position relative to the body, which impacts line-of-sight and the creeping wave.

Verification of the phantom measurement is performed using CST simulation, using the CST phantom setup mentioned previously. The motion capture for the phantom model performing the arm swing at 915MHz wearing antennas on the chest/left wrist (front) is used to control the CST phantom model's motion. The simulation is performed at 10fps at 915MHz and the S-parameters are obtained. Using the frame rate, the time scale for the simulated results can be determined, allowing for the simulation to be plotted against time. Figure 3.6 shows S_{21} vs time at 915MHz for the phantom model measurement compared to the phantom model CST simulation with the monopoles in the chest/left wrist (front) configuration. The peak and dip pattern for the phantom measurement and simulation show good agreement, with the same periodicity and pattern. The S_{21} fluctuation pattern shows that the signal drops as the arm swings behind the torso (0.8s to 1.4s), increases as the arm moves forward in front of the torso (1.4s to 2.1s), then stays relatively flat while the arm stays in front of the torso (2.1s to 3.8s), with a slightly more defined M-shape in the simulation than the measurement.

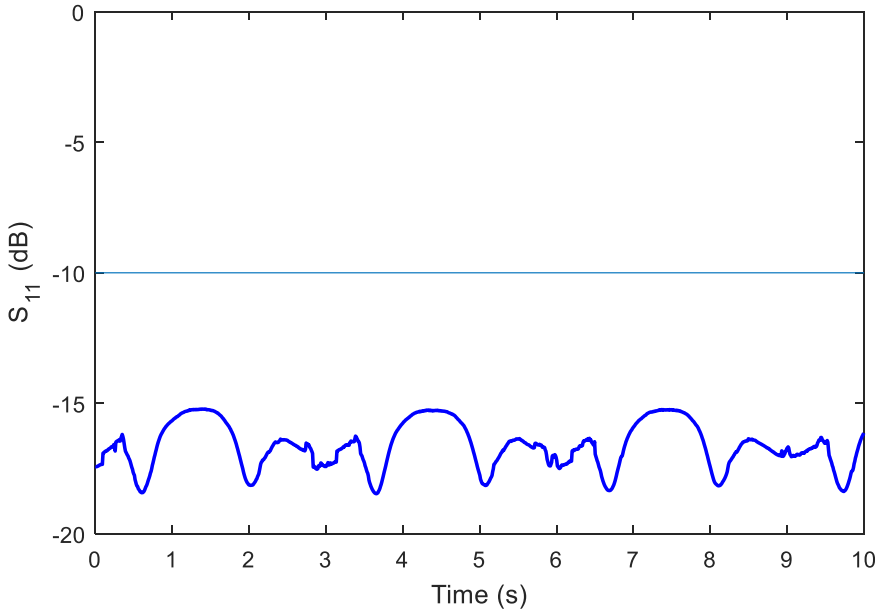

Figure 3.4. S_{11} vs time for the wrist antenna when worn on the phantom model performing an arm swinging motion with antennas in the chest/left wrist (front) configuration.

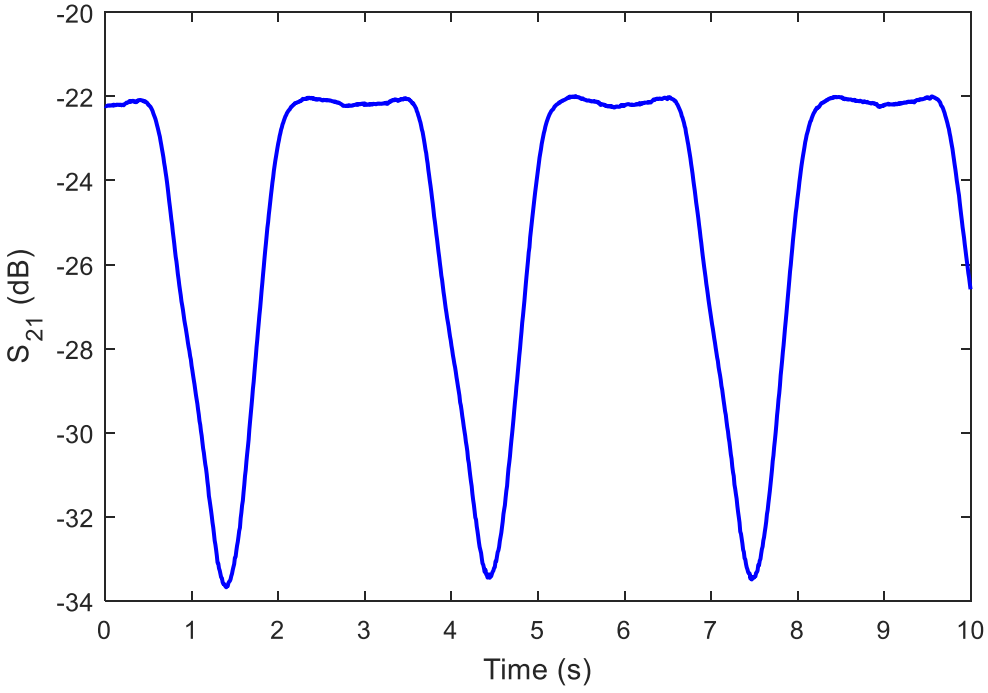

Figure 3.5. S_{21} vs time for the phantom model with antennas on the chest/left wrist (front) with 915MHz monopole antennas.

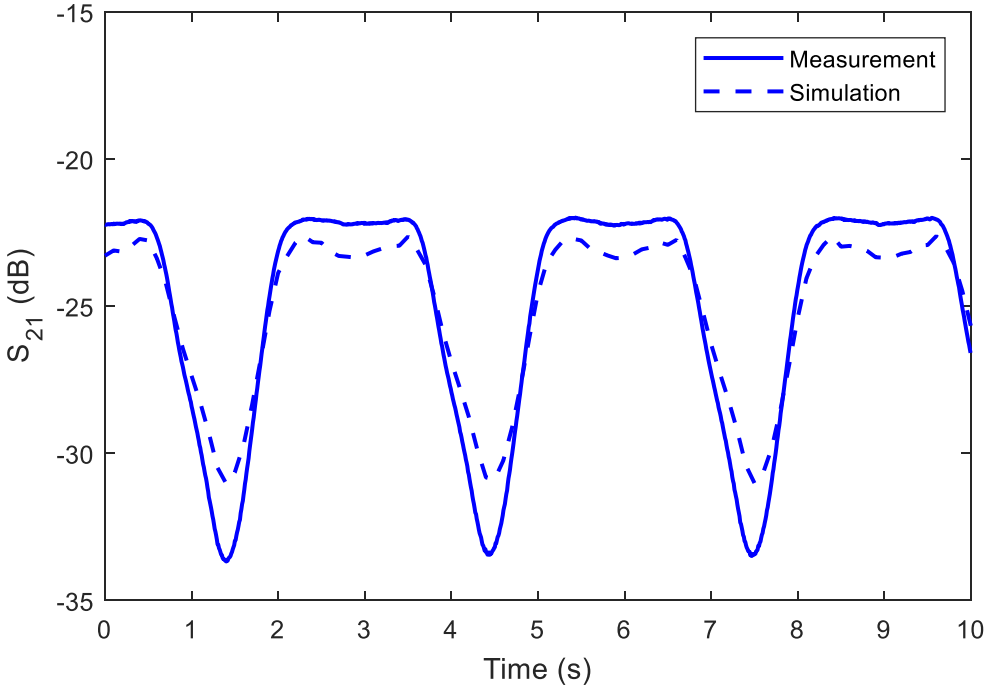

Figure 3.6. S_{21} vs time for the phantom model measurement and simulation with antennas on the chest/left wrist (front) with 915MHz monopole antennas.

Additional verification of the phantom model's ability to accurately represent human body effects on dynamic on-body EM wave propagation was performed by comparing the phantom model measurement to human volunteer measurement. The sizes of the phantom model and the human volunteer can be seen in Table 3.1. The phantom model is similar to the size of an actual human, but there is great variance in human body sizes, which is why the modular design of the phantom is useful for future studies on parameters such as body size. The human volunteers performed the same arm swinging motion at a 3.0s cadence following the beat of a metronome to improve arm swing consistency and for fair comparison with the phantom. The same antenna placement was used for the human measurement as well. Figure 3.7 shows S_{21} vs time at 915MHz comparing the phantom model measurement and human volunteer measurement for the

chest/left wrist (front) antenna configuration. It is apparent that the human measurement data shares the same pattern and periodicity for S_{21} fluctuations as the phantom model, with a clear peak and dip pattern. The human data shows a peak and dip pattern with a slight M-shaped pattern occurring during the S_{21} peak timings. An example cycle can be defined as the S_{21} decreasing from 0.5s to 1.5s, increasing from 1.5s to 2.5s, and showing the M-shaped fluctuation during the S_{21} peak from 2.5s to 3.5s. The similarity in pattern and periodicity suggests the phantom model has a similar effect on on-body EM wave propagation as an actual human body in motion, though there is some discrepancy in S_{21} magnitude, where it can be seen that the S_{21} dips for the phantom stay above -35dB, while the human measurement shows the S_{21} dips in the -45dB to -50dB range.

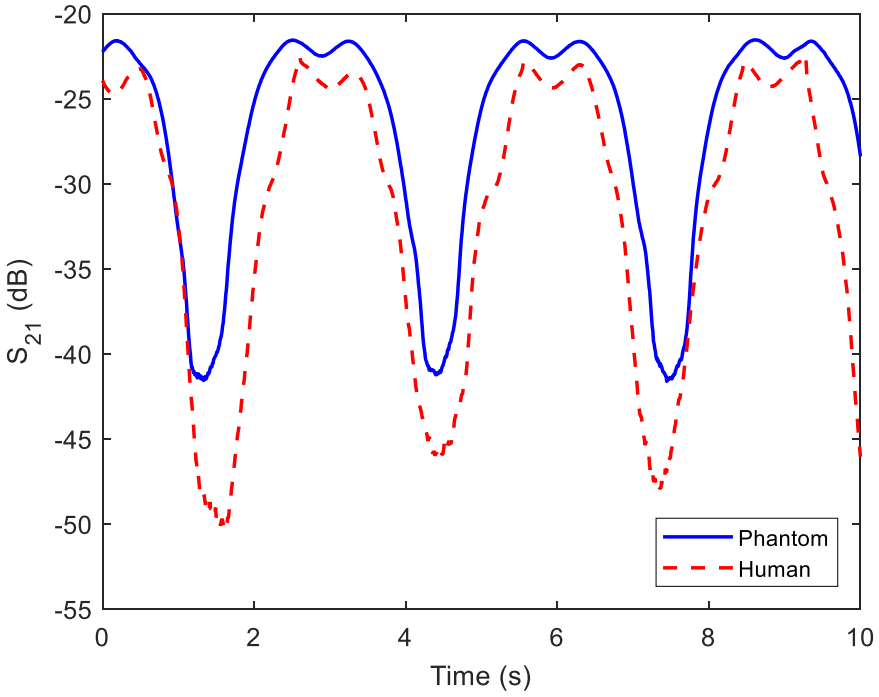

Figure 3.7. S_{21} vs time for the phantom model measurement and human volunteer measurement with antennas on the chest/left wrist (front) with 915MHz monopole antennas.

The monopole testing also demonstrates one of the phantom model's advantages over human measurement, which is consistency. Figure 3.8 shows S_{21} vs time for three trial data sets of the phantom model performing the arm swing with the 915MHz monopoles in the chest/left wrist (front) configuration. The three data sets show the same pattern and periodicity, in addition to negligible differences in magnitude. On the other hand, Figure 3.9 shows S_{21} vs time for three trial data sets of the human volunteer performing the arm swing with the 915MHz monopoles in the chest/left wrist (front) configuration, which shows much less consistency in magnitude between trials, while still showing the same pattern and periodicity.

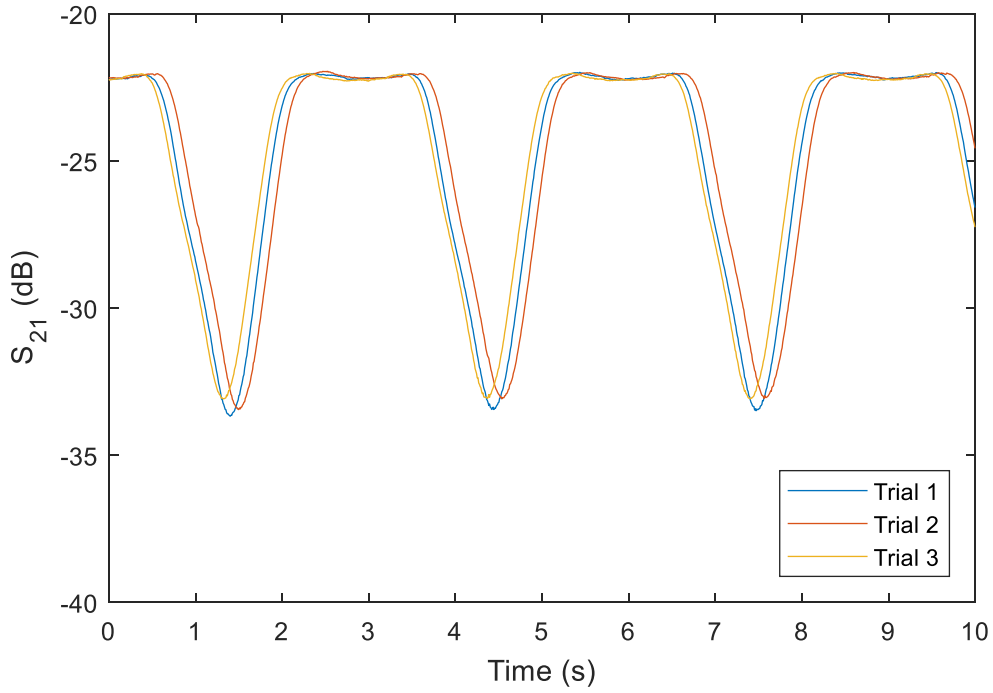

Figure 3.8. S_{21} vs time for three trials of phantom model measurement with antennas on the chest/left wrist (front) with 915MHz monopole antennas.

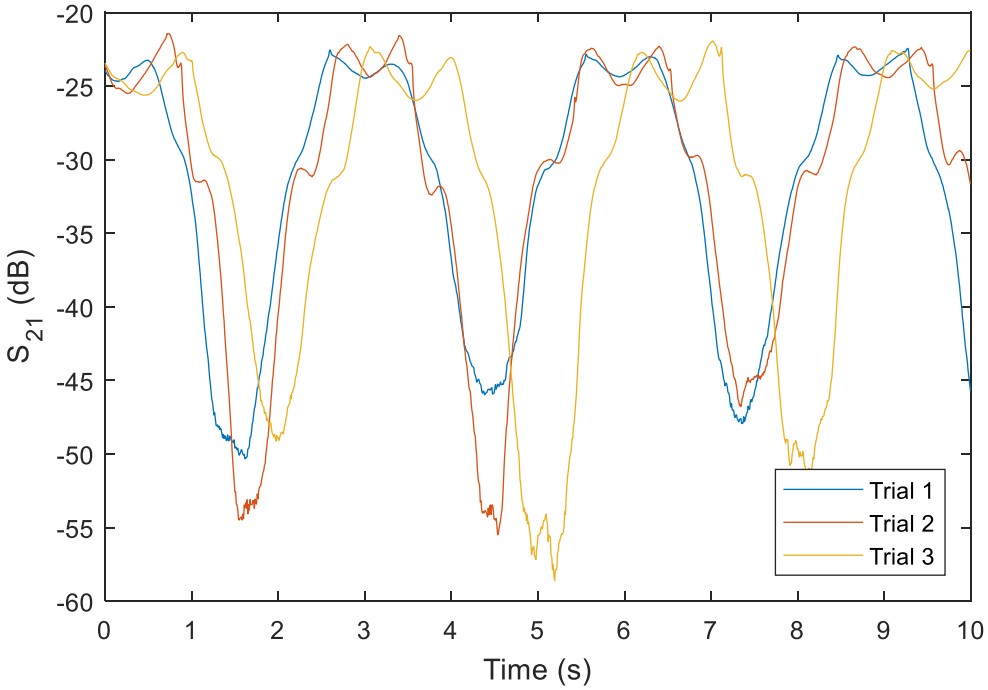

Figure 3.9. S_{21} vs time for three trials of human volunteer measurement with antennas on the chest/left wrist (front) with 915MHz monopole antennas.

Table 3.1. Comparison of phantom and human volunteer size for monopole testing.

Body Part	Phantom Model	Human Volunteer 1	Human Volunteer 2	Human Volunteer 3
Torso Length (cm)	53.7	55	57	54
Torso Circumference (cm)	102.9	92.7	87.8	111.8
Arm Length (cm)	68.6	56	59	57.5
Arm Circumference (cm)	33	27.5	25.3	30.6

Further analysis can be performed if the data is arranged to compare S_{21} vs arm angle. The arm angle is calculated using the motion capture marker data on the phantom and human arms, as mentioned previously. Figure 3.10 shows arm angle vs time for the phantom model and the human volunteer during the 915MHz measurement with monopoles worn on the chest/left wrist (front). The arm swing angle is the angle formed between the arm and the torso (vertical) as seen from the sagittal plane. The positive arm

swing angles refer to when the arm is in front of the torso (shoulder flexion) and the negative arm angles refer to when the arm is behind the torso (shoulder extension), with a zero angle meaning the arm is at the side of the body and perpendicular to the ground. This plot confirms that the phantom model and human volunteer are performing the arm swing motion at a similar cadence due to the matching of the peak and minimum arm swing angles. The motions are also consistent between the phantom and human, showing near 3.0s between peaks and dips in arm angle. Additionally, the phantom and human are shown to have a similar arm swing range, with the human moving further when the arm is in front of the torso.

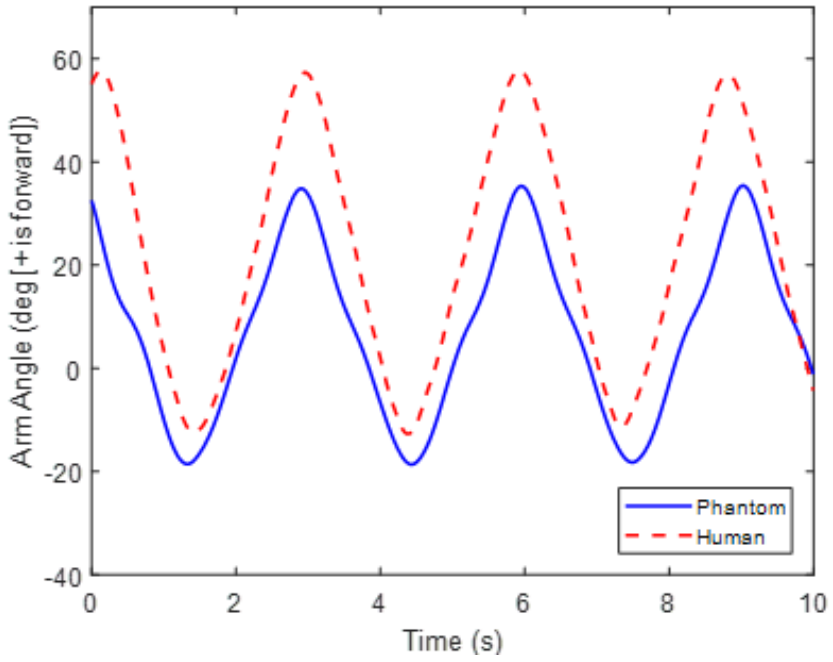

Figure 3.10. Arm angle vs time from phantom model measurement and human volunteer measurement with antennas on the chest/left wrist (front) with 915MHz monopole antennas.

Plotting S_{21} vs arm angle gives a better idea of how the position of the arm changes the signal strength between the on-body antennas. Figure 3.11 shows the comparison of S_{21} vs arm angle for the 915MHz antenna on chest/ left wrist (front) configuration. The S_{21} data being shown is the same as In Figure 3.7; however, additional human volunteer data is added and the analysis against angle significantly changes how the data is presented. Looking at the arm angle of the phantom model and the human volunteers gives us insight into the body positions during the arm swinging motion that cause the greatest losses in S_{21}. This information can be used to assist in designing optimized antenna, such as directional antenna or antenna with alternating polarities. The pattern of the S_{21} vs angle plot can provide us with the vital information. Figure 3.11 shows that the S_{21} vs angle creates a fairly simple curve shaped pattern. The curve consists of dips in S_{21} that occur when the moving arm is behind the body during the swing motion, as demonstrated by the negative arm angles having the lowest S_{21} values, for both the phantom and human volunteer. The S_{21} is higher at positive arm angles, which is when the arm is in front of the torso, with a near plateau at higher arm angles, which is again demonstrated by the phantom and the human volunteer. This suggests the phantom model motion does have a similar effect on S_{21} as human body motion. Additionally it can be noted that the phantom model data is more consistent than the human volunteer's data, as each of the cycles begins to overlap very heavily when compared to the human data, where each cycle has more variance, showing less overlap as arm angles repeat over multiple cycles. Additionally, it can be seen that the same arm swing angles can yield different S_{21} values for the same phantom measurement trial or human volunteer. The data shows that these different S_{21} values also occur at different

phases of the arm swing, meaning the S_{21} at -5deg can vary if the angle occurs the forward swing compared to the back swing. This suggests there is a directional effect, meaning the direction of the arm swing can affect the antenna transmission. The comparison of phantom and human data shows the difference in mean S_{21} between the phantom measurement and the measurement of the three human volunteers for the 915MHz monopoles worn on the chest/left wrist (front) is 4.29dB, which is similar to or better than the difference between measurement and simulation in previous studies, such as up 3.8dB in [21] and 5dB in [25]. This suggests the discrepancy between the phantom and human measurement is acceptable, as previous works that compared discrepancies between human measurement and computer models have shown similar agreement. The S21 fluctuation pattern is more important for determining where the weaknesses in signal during motion occur, meaning matching the fluctuation pattern between the phantom and human is more important than exact magnitude matching. Pattern matching gives critical information that can used for antenna optimization, such as knowing when to focus the antenna radiation or how to modify radiation patterns to better suit different motions and antenna placements. Due to the match in S_{21} fluctuation pattern and magnitude, the phantom is shown to be similar to the human volunteers in terms of effect on EM wave propagation due to motion.

Further analysis can be performed if the data is arranged to compare average S_{21} vs % cycle. Percent cycle refers to the percentage of an arm swing cycle that has been completed, meaning the average S_{21} at 50% cycle is the average value of S_{21} at the time when half the arm swing has been completed. The comparison of average S_{21} vs percent cycle gives a clearer view of the S_{21} pattern that can be seen in S_{21} vs time by eliminating

any time inconsistencies between cycles and averaging out the S_{21} for each cycle.Figure 3.12 compares the phantom and human measurement data with 915MHz antenna on chest and left wrist (front) data set using average S_{21} vs percent cycle. This view gives a better idea of what each cycle looks like with a normalized x-axis, so any time variances that can occur, usually in human measurement, can be reduced. This comparison shows that the cycle has a plateau with a slight M-shape (0% to 60%, followed by a sharp drop in S_{21} (60% to 80%), with a rise at the end (80% to 100%). The use of average S_{21} vs percent cycle also makes it very clear what pattern each cycle has, which allows for easier comparison between phantom and human data. Also, the periodicity is normalized so even if one cycle was 2.9s and the other was 3.1s, the use of percent cycle normalizes this discrepancy, allowing for the actual S_{21} pattern of the cycle to be apparent. This percent cycle comparison also shows strong agreement in pattern, periodicity, and magnitude when comparing the phantom model and the human volunteer.

A representative body motion, the arm swing, and antenna placement with relevant uses, chest and wrist, at an industrial, scientific, and medical (ISM) frequency frequency, 915MHz, was tested using the phantom model and multiple human volunteers. Motion capture and antenna signal data were collected simultaneously, allowing for a thorough comparison of phantom and human measurement data. Additionally, a computer simulation model of the phantom was created in CST and performed the same motions in simulation as in measurement by using motion capture data. The S_{21} data was compared in three ways: time, arm angle, and percent cycle. All three comparisons showed good agreement between the phantom model and human volunteer measurement. The phantom simulation also agreed with the phantom measurement. This agreement

between phantom measurement, simulation, and human volunteer measurement suggests the phantom model does have a similar effect on S_{21} as the human body, even during motion activities.

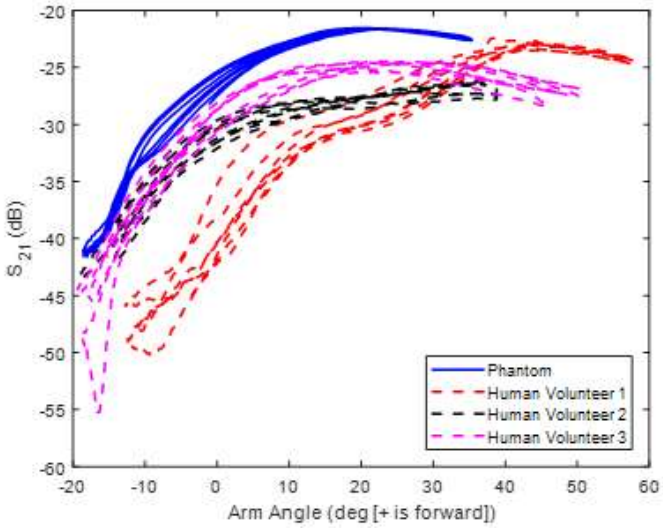

Figure 3.11. S_{21} vs arm angle for the phantom model measurement and human volunteer measurement with antennas on the chest/left wrist (front) with 915MHz monopole antennas.

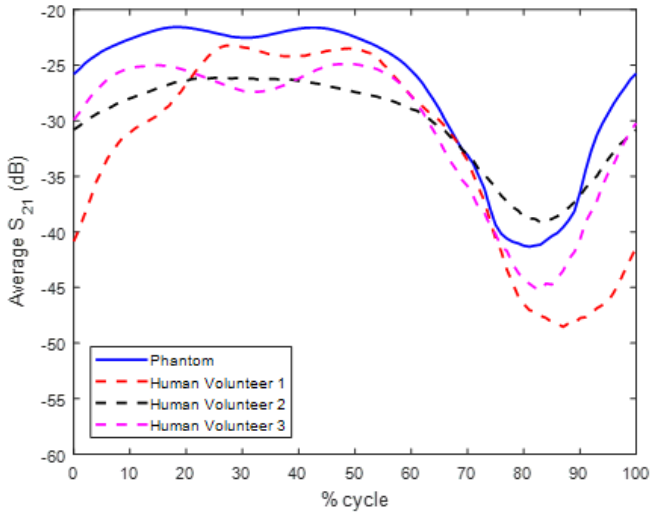

Figure 3.12. Average S_{21} vs % cycle for the phantom model measurement and human volunteer measurement with antennas on the chest/left wrist (front) with 915MHz monopole antennas.

Summary

The phantom model was validated using computer simulation and measurement methods. The phantom model was used for measurement wearing 915MHz monopole antennas on the chest/left wrist (front). The motion data from the measurement was used to perform CST simulation of the phantom model, which showed good agreement with the measurement. Measurement with human volunteers was also performed and showed good agreement with the phantom measurement, as seen in similar ranges of S_{21} differences between human measurement and other models from previous studies and more importantly, the S_{21} fluctuation patterns were similar. The combination of pattern matching and similarities in magnitude for S_{21} verified the phantom model's effectiveness in capturing body motion effects on on-body EM wave propagation.

CHAPTER FOUR

Phantom Model Parametric Study

Based on the verification of the phantom model using the bridge monopole antennas, the phantom model was shown to have a similar effect on EM wave propagation as actual human bodies, which suggests the phantom can be used for studies on on-body wave propagation. The study of on-body EM wave propagation can benefit greatly from understanding how certain factors may affect wearable antenna performance in an isolated manner, which can help see which individual factors have the greatest impact. As mentioned previously, some of the factors that one may want to test cannot be easily changed for a human volunteer, such as body dielectric properties. The phantom model's modularity allows us to change these parameters and observe how the S_{21} patterns and magnitudes change with the different parameters. This can allow us to discern which parameters have the greatest impact and potentially find how to reduce losses in S_{21} during wearable device scenarios. Thus, a parametric study was performed to determine what parameters of the human body may have the most significant impact on EM wave propagation. The parameters addressed in this study were antenna operating frequency, antenna placement configuration, and body dielectric properties. The portions of this parametric study that involve comparison with human measurement involved measurement with three human volunteers.

Antenna Operating Frequency

The antenna operating frequency is an important parameter to test because antenna frequency impacts antenna size and could potentially change the fluctuations in antenna signal caused by body motion. Higher frequency antennas are generally smaller than low frequency, but can have greater loss. Both of these factors are critical for on-body antenna design, and thus antenna frequency must be explored.

The antenna frequencies tested are 433MHz, 915MHz, and 2.45GHz, which are in the ISM frequency band, which is used for medical purposes. The measurement methodology again compared the phantom model to human volunteer data, which allows for additional verification of the phantom model's ability to emulate the effect the human body has on EM wave propagation.

The antenna placement used for the testing of antenna operating frequency is chest and left wrist (front) antenna. This parametric study uses a 3.0s arm swing cadence for both the phantom model through motor control and the human volunteers using a metronome. The arm swing angle range of the phantom is set to a range that is comparable with human volunteer range of motion.

Bridge monopole antennas are used for varying the antenna operating frequency. The copper wire's length is changed, allowing for resonance at the desired frequencies of 433MHz, 915MHz, and 2.45GHz. The same ground plane from Chapter 3 is used for all three monopole antenna frequencies. The large variance in antenna size change due to frequency is very apparent with the monopole antenna, where the 433MHz antenna is 17.3cm long compared to 3.1cm long for the 2.45GHz monopole. The difference in

antenna size is a key factor for using higher antenna frequencies and understanding how higher antenna frequencies will be affected by human body motion.

Figures 4.1, 4.2 and 4.3 show S_{21} vs time for the arm swinging motion with antenna on the chest/left wrist (front) at 433MHz, 915MHz, and 2.45GHz for the phantom model and human volunteers. There are several key points that this comparison shows. The first is the noticeable drop in S_{21} as frequency increases, where the overall S_{21} is higher at 433MHz, as seen in Figure 4.1, than at 915MHz, which can be seen in Figure 4.2, and 2.45GHz, which can be seen in Figure 4.3. Another point is the similarity of the S_{21} pattern when comparing all three frequencies. The M-shape pattern is seen for each frequency, where there are sharp drops and plateaus with light M-shape patterns throughout the arm swing cycle. This shows that the lower frequency antennas do have less loss in antenna signal strength than higher antennas during on-body scenarios. Additionally, it suggests that that the antenna frequency does not have a significant effect on the S_{21} fluctuation patterns caused by human body motion. Another note is that the discrepancy is magnitude between the phantom and human data is still present at 433MHz and 2.45GHz, however, Figures 4.1, 4.2 and 4.3 still clearly show that the pattern and periodicity are in good agreement between phantom and human measurement, with a repeated M-shaped peak and dip pattern repeating over time. Additionally, the M-shape is strongest at 2.45GHz, where Figure 4.3 shows that the dip in the M-shape has a magnitude of 7dB for the phantom, which is greater than the dips in Figures 4.1 and 4.2, which show the dip in S_{21} for the M-shape as less than 2dB for the phantom.

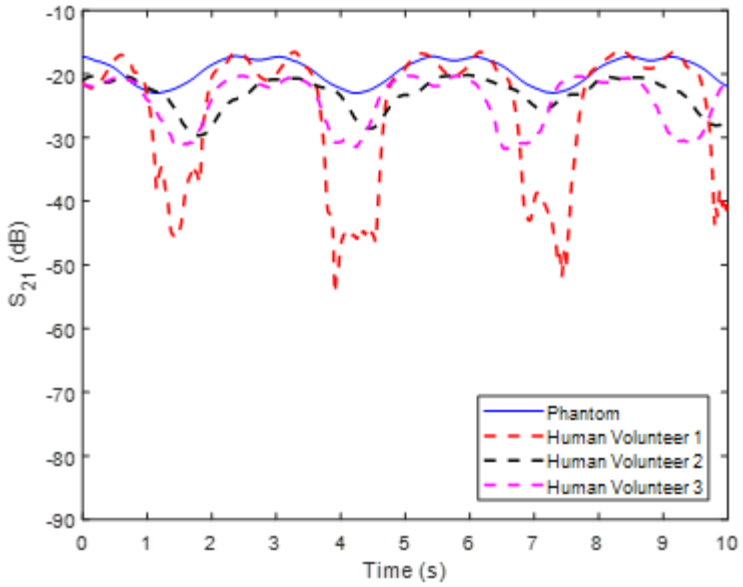

Figure 4.1. S_{21} vs. time at 433MHz for phantom model measurement and human measurement with monopole antennas on the chest/left wrist.

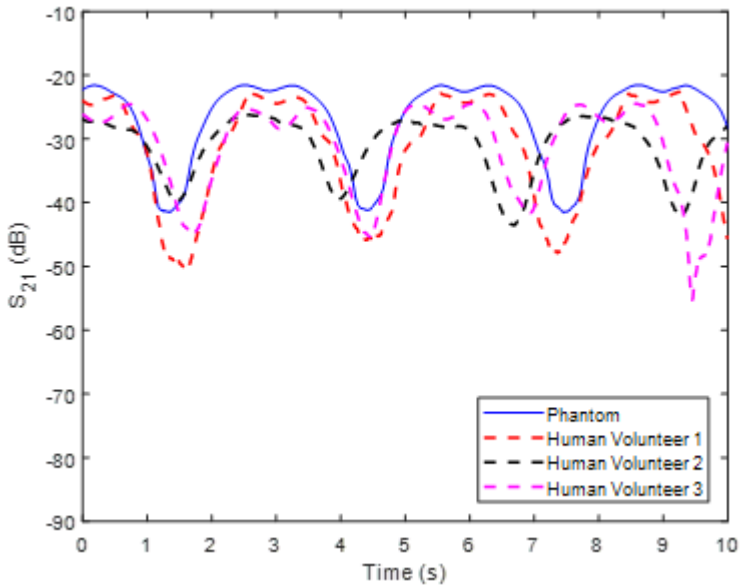

Figure 4.2. S_{21} vs. time at 915MHz for phantom model measurement and human measurement with monopole antennas on the chest/left wrist.

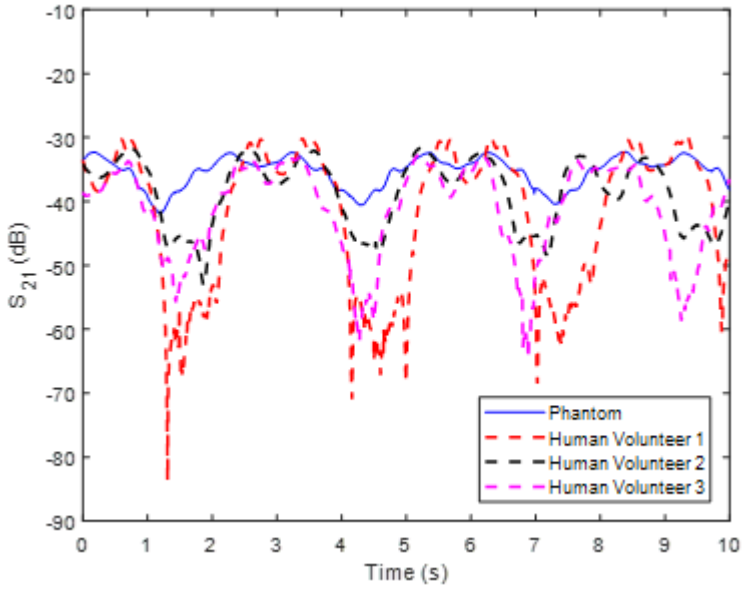

Figure 4.3. S_{21} vs. time at 2.45GHz for phantom model measurement and human measurement with monopole antennas on the chest/left wrist.

Figures 4.4, 4.5, and 4.6 show the comparison of S_{21} vs angle for the same arm swinging motion with antenna on the chest/ left wrist (front) at 433MHz, 915MHz, and 2.45GHz for the phantom model and human volunteers. The overall trend shown by the Figure 4.5 at 915MHz shows that the lowest S_{21} values occur during the negative arm angles, which means the greatest dips in S_{21} occur when the arm is behind the body, which was described previously in Figure 3.11. The peak S_{21} values occur during positive arm angles, which means the strongest antenna transmission occurs when the arm is in front of the body. This S_{21} trend can be seen at 433MHz in Figure 4.4 for both the phantom and human measurement data, where the greatest magnitude discrepancy between the phantom and human can be seen at negative arm angles, where the human S_{21} has lows near 55dB, while the phantom S_{21} lows are -25dB. Despite the negative arm angle difference in magnitude, the overall pattern of lower S_{21} at negative arm angles is

present for both the phantom and human. The S_{21} trend also continues in Figure 4.6, which shows the 2.45GHz data. The lowest S_{21} values are reached at negative arm angles, showing the S_{21} has greater loss when the arm is behind the body. The S_{21} is generally higher when at positive arm angles, showing that there is less loss in S_{21} when the antenna is in front of the body. However, it can be seen that during positive arm angles, the S_{21} does begin to decrease at the highest arm angles in Figure 4.6, which can be seen from 17deg to 30deg for the phantom and 35deg to 57deg for the human volunteer. This shows that the M-shape pattern in the overall S_{21} peak trend occurs when the arm is in front of the torso and is caused by the S_{21} decreasing at the highest arm angles then increasing again as the arm begins to move towards the torso again.

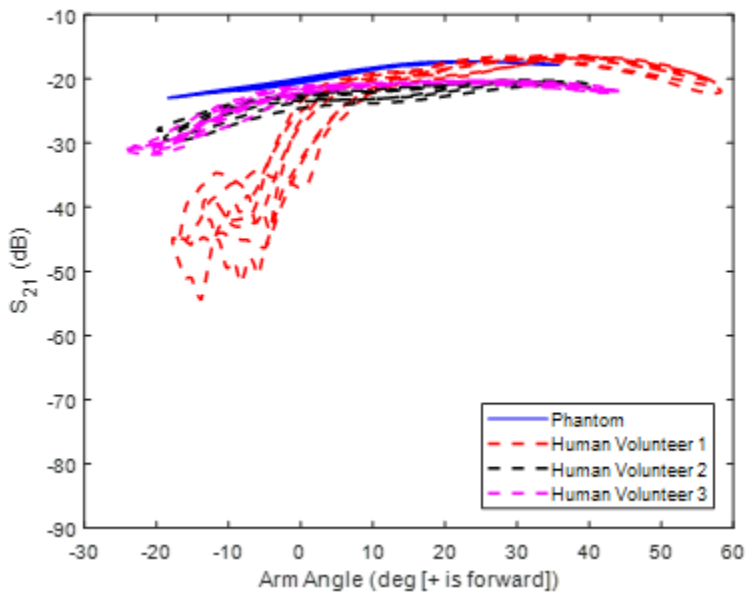

Figure 4.4. S_{21} vs. angle at 433MHz for phantom model measurement and human measurement with monopole antennas on the chest/left wrist (front).

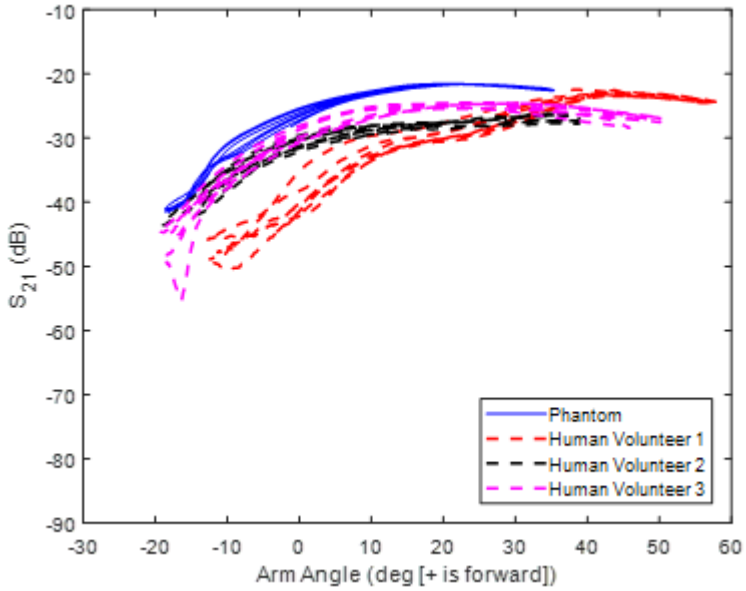

Figure 4.5. S_{21} vs. angle at 915MHz for phantom model measurement and human measurement with monopole antennas on the chest/left wrist (front).

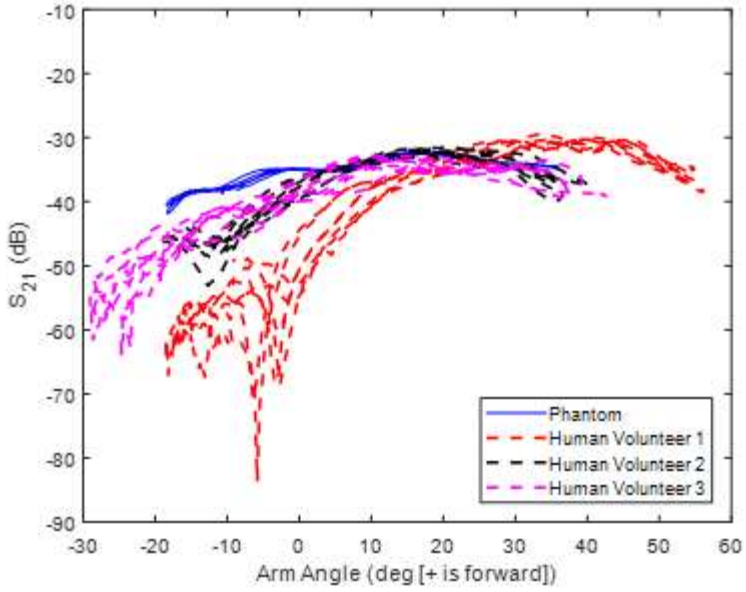

Figure 4.6. S_{21} vs. angle at 2.45GHz for phantom model measurement and human measurement with monopole antennas on the chest/left wrist (front).

Antenna Placement

Antenna placement is a parameter that must be investigated because wearable devices can be potentially placed on any part of the body; however, the position on the body will have an impact on the key wave propagation mechanisms, such as line-of-sight and the creeping wave. Also, some placements may be more convenient or comfortable for the wearer to implement. Understanding how different antenna positions affect EM wave propagation will be helpful for optimizing on-body antenna design.

Antenna performance during an arm swinging motion were used to assess various antenna placement configurations. The antennas are tested in three placement configurations: chest/ left wrist (front), chest/left wrist (back), and both wrists (front). These placements are chosen because they can represent possible real-world placements of WBAN sensors, such as a smartwatch being worn at the wrist communicating with a device worn on the torso. 915MHz monopole antennas were used to test the antenna placement configurations. The arm swing speed was set to a 3.0s cadence for the phantom and human volunteer.

Figures 4.7, 4.8, and 4.9 show S_{21} vs time at 915MHz comparing the phantom and human measurement for the chest/left wrist (front), chest/left wrist (back), and both wrists (front) antenna configurations. Overall, there is good agreement between the phantom and human data for all three antenna positions, as seen by the similar patterns and periodicities seen in the S_{21} fluctuations for all three antenna positions. There is a noticeable effect in the S_{21} fluctuation pattern caused by changing the antenna position. Figure 4.7 and 4.9 show the chest/left wrist (front) and both wrists (front) configurations. A comparison between the two configurations shows that both share the M-shaped peak

and dip factor, with some discrepancies in overall maximum and minimum S_{21} magnitude and the magnitude of the dip in the M-shape. However, looking at Figure 4.8, it can be seen that the chest/left wrist (back) antenna configuration has a significantly different S_{21} fluctuation pattern, with the peak and dip pattern changing. The peak timing no longer has an M-shape. Instead there are additional fluctuations in S_{21} as the S_{21} decreases and again as the S_{21} increases. This can be seen where there is a fluctuation in S_{21} at 1s for the phantom data set as the S_{21} is decreasing and then another fluctuation at 2s when the S_{21} is increasing. A similar trend can be seen at 1s and 2.5s for the human data set. This shows that antenna placement can change the S_{21} fluctuation pattern during body motion.

Figures 4.10, 4.11, and 4.12 show S_{21} vs angle at 915MHz comparing the phantom and human measurement for the chest/left wrist (front), chest/left wrist (back), and both wrists (front) antenna configurations. Figures 4.10 and 4.12 shows similar trends for the chest/left wrist (front) and both wrists (front) configurations, with the higher S_{21} occurring at positive arm angles and lower S_{21} at negative arm angles, showing how there is less loss in S_{21} in front of the torso for these antenna placements. Figure 4.11 also shares this overall S_{21} trend of high S_{21} at positive arm angles. However, there is a difference in pattern from -10deg to 10deg, for both the phantom and human, when compared to Figures 4.10 and 4.12. The S_{21} increases slightly before decreasing again, which shows that the fluctuations that occur as the overall S_{21} trend increase and decrease occur at the arm position around 10deg. Figures 4.10, 4.11, and 4.12 show how the S_{21} behaves differently at different arm positions when the antenna position changes. Additionally, there is good agreement between the phantom and human measurement data for all three antenna placement configurations tested.

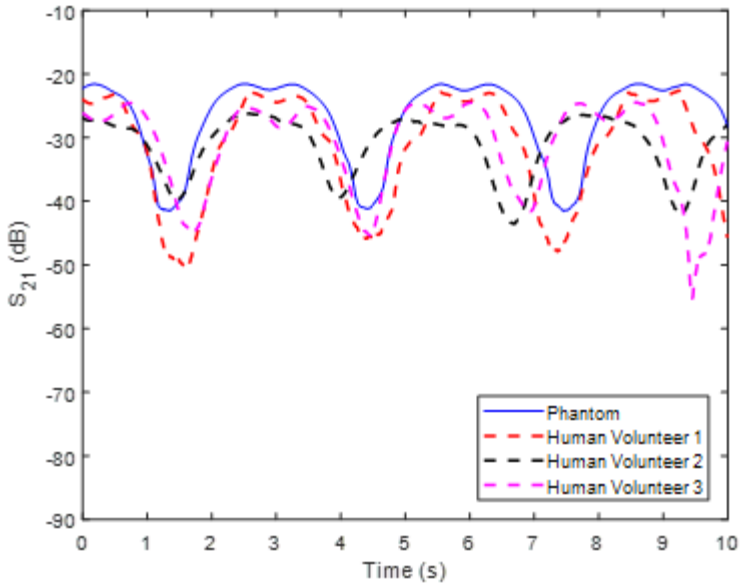

Figure 4.7. S_{21} vs. time at 915MHz for phantom model measurement and human measurement with monopole antennas on the chest/left wrist (front).

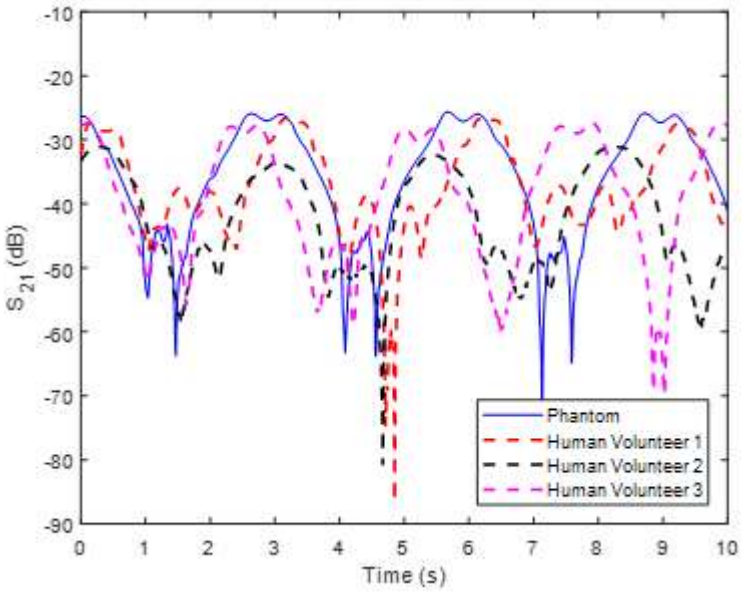

Figure 4.8. S_{21} vs. time at 915MHz for phantom model measurement and human measurement with monopole antennas on the chest/left wrist (back).

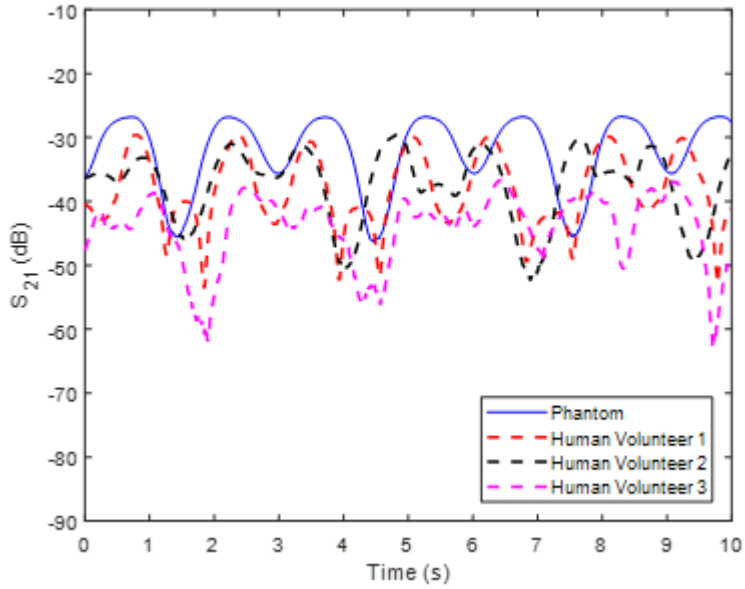

Figure 4.9. S_{21} vs. time at 915MHz for phantom model measurement and human measurement with monopole antennas on the both wrists (front).

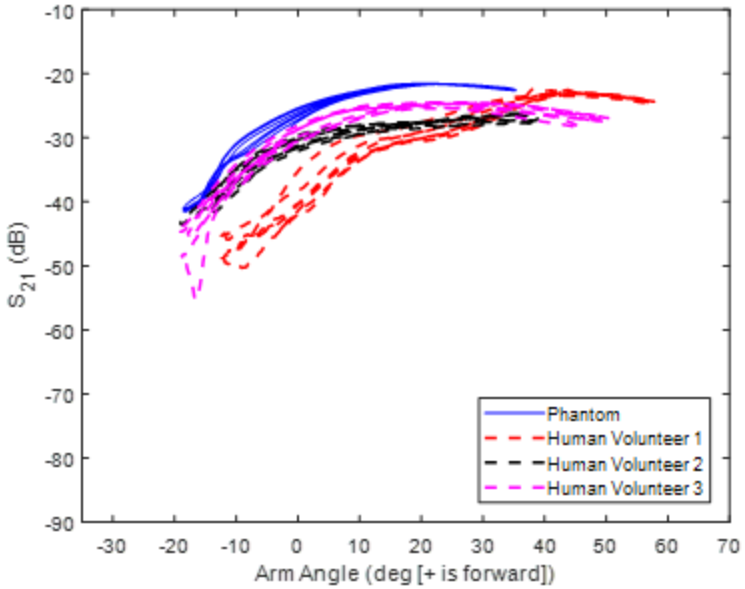

Figure 4.10. S_{21} vs. angle at 915MHz for phantom model measurement and human measurement with monopole antennas on the chest/left wrist (front).

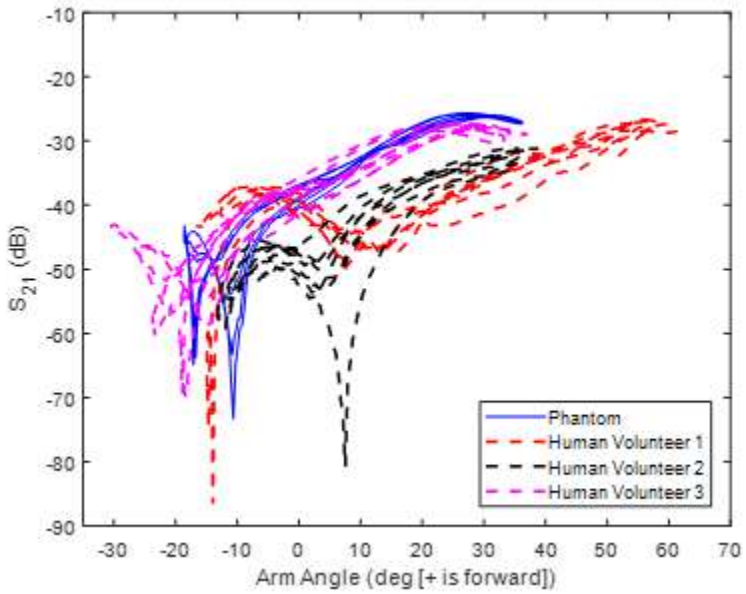

Figure 4.11. S_{21} vs. angle at 915MHz for phantom model measurement and human measurement with monopole antennas on the chest/left wrist (back).

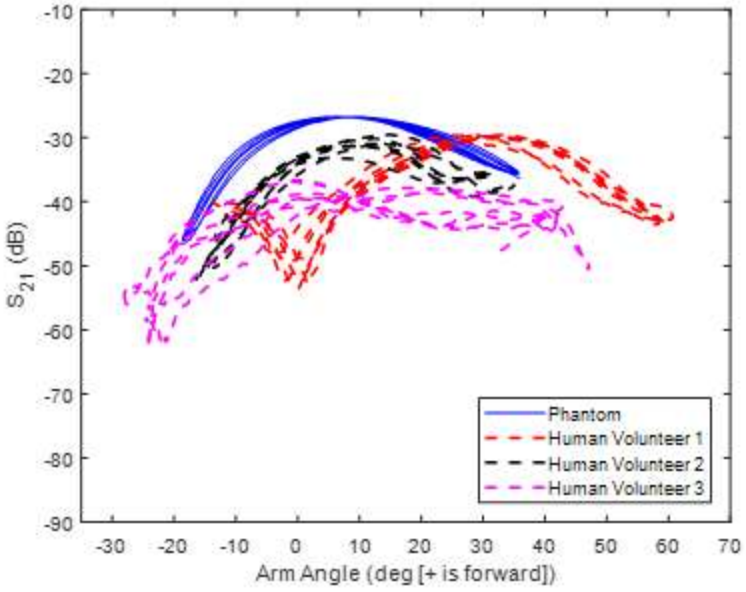

Figure 4.12. S_{21} vs. angle at 915MHz for phantom model measurement and human measurement with monopole antennas on the both wrists (front).

Body Dielectric Properties

Variations in body dielectric property can be caused by different body compositions, such as different percentages of muscle and fat for different people. The phantom model allows for this property to be varied easily, which cannot be done with human volunteers. The phantom model also gives the opportunity to isolate motion effects from body effects by changing the dielectric property to essentially being air. The phantom model's plexiglass shell is essentially electrically invisible, so the empty phantom model does not have significant effects on EM wave propagation; however, the arms can still swing and antenna can still be placed. This allows for the antenna to almost "float" in motion, allowing for analysis of the motion and positional effect on EM wave propagation separately from having an actual body present. This has the potential to isolate motion effects from body effects on S_{21} and to see how the dielectric properties of the body can affect S_{21}. The difference in body dielectric properties was tested by comparing the phantom model filled with muscle tissue simulating solution and the phantom model being empty.

Initially, the phantom model was tested to ensure that the empty phantom model would have a similar effect on S_{21} as free space. This was performed by comparing the effect of free space, the empty phantom torso, and the phantom torso filled with muscle tissue simulating solution on S_{21} when placed between two 915MHz bridge monopole antennas. The test setup can be seen in Figures 4.13, 4.14, and 4.15, where Figure 4.12 shows the test of having free space between the antennas, Figure 4.14 shows the test of the empty phantom between the antennas, and Figure 4.15 shows the test of the phantom filled with muscle tissue simulating solution between the antennas.

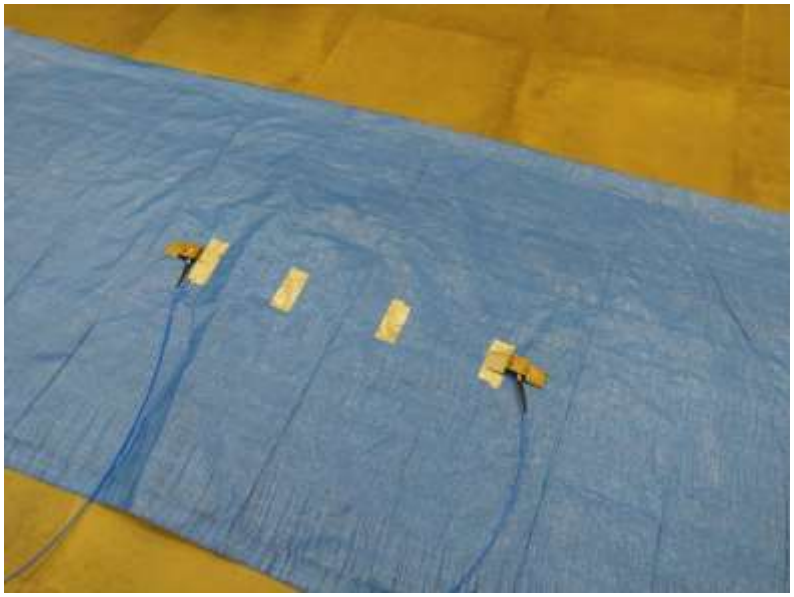

Figure 4.13. Two 915MHz monopole antennas placed on the floor with free space in between them.

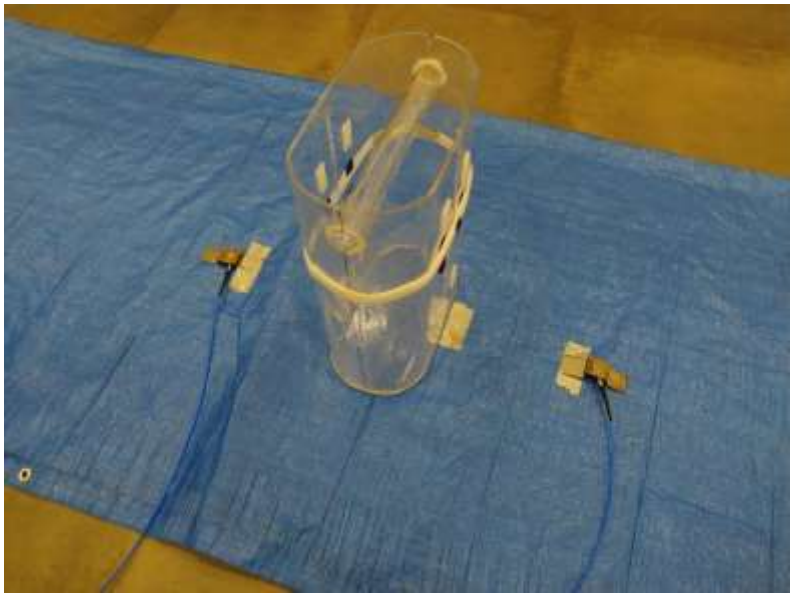

Figure 4.14. Two 915MHz monopole antennas placed on the floor with the empty phantom torso in between them.

Figure 4.15. Two 915MHz monopole antennas placed on the floor with the phantom torso filled with muscle tissue simulating solution in between them.

Figure 4.16 shows S_{21} vs time at 915MHz when free space, the empty phantom, and the phantom filled with muscle tissue simulation solution are placed between the monopole antennas. The S_{21} is approximately -25dB with free space between the antennas. The S_{21} is approximately -25dB the empty phantom model is between the antennas. The S_{21} stays between -35dB and -40dB when the phantom model filled with muscle tissue simulation solution is between the antennas. There are two key points that this demonstrates, which are that the empty phantom had a similar effect on S_{21} as free space and that the presence of a body, such as the phantom filled with muscle tissue solution, causes considerable losses in antenna transmission. The confirmation of the similarity between the empty phantom and free space allowed for the testing of dielectric properties on motion through the use of the empty and the filled phantom model.

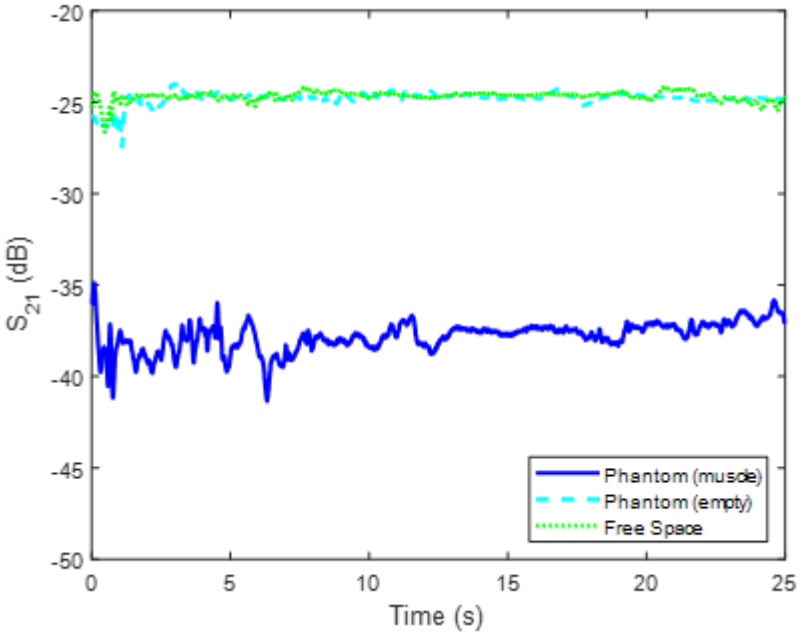

Figure 4.16. S_{21} vs time for two 915MHz monopole antennas placed on the floor with three different mediums in between them: free space, an empty phantom torso, and a phantom torso filled with muscle tissue simulating solution.

Figures 4.17, 4.18, and 4.19 show S_{21} vs time at 915MHz for the phantom model filled with muscle tissue simulation solution and the phantom while empty, for the chest/left wrist (front), chest/left wrist (back), and both wrists (front) antenna configurations. Figure 4.17 and 4.19 show that the peak and dip timings for the chest/left wrist (front) and both wrists (front) antenna configurations are flipped when comparing the filled and empty phantom. This change in trend is caused by changes in line-of-sight, which significantly impact the wrist (front) antenna configurations, where the torso would normally block the line-of-sight between the chest and wrist (front) when the arm is behind the body. For example, in Figure 4.17 at 1.5s, the filled phantom is in an S_{21} dip timing, while the empty phantom is in an S_{21} peak timing. Similarly, in Figure 4.19 at 1.5s, the filled phantom is in an S_{21} dip timing, while the empty phantom is in an S_{21} peak

timing. On the other hand, the peak and dip timings match between filled and empty phantom in Figure 4.18, which shows the chest/left wrist (back) antenna configuration. There are some differences in the S_{21} fluctuation pattern, such as the filled phantom showing small fluctuations, such as at 0.8s and 2.0s, while the empty phantom stays at peak S_{21} values longer, which can be seen when comparing the empty to filled phantom from 2.0s to 4.0s. Despite these discrepancies, the overall S_{21} trend is the same between the filled and empty phantom models for the chest/left wrist (back) configuration, unlike chest/left wrist (front) and both wrists (front).

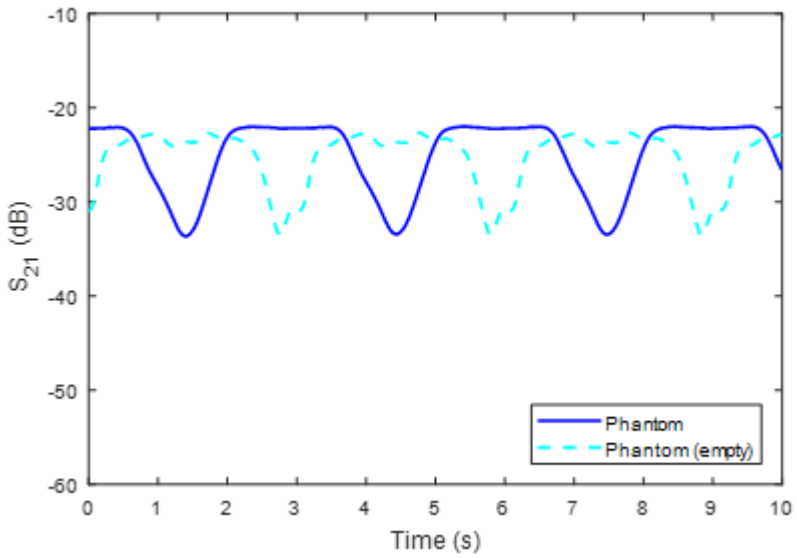

Figure 4.17. S_{21} vs time at 915MHz for the phantom filled with muscle tissue simulating solution and the empty phantom with monopole antennas on the chest/left wrist (front).

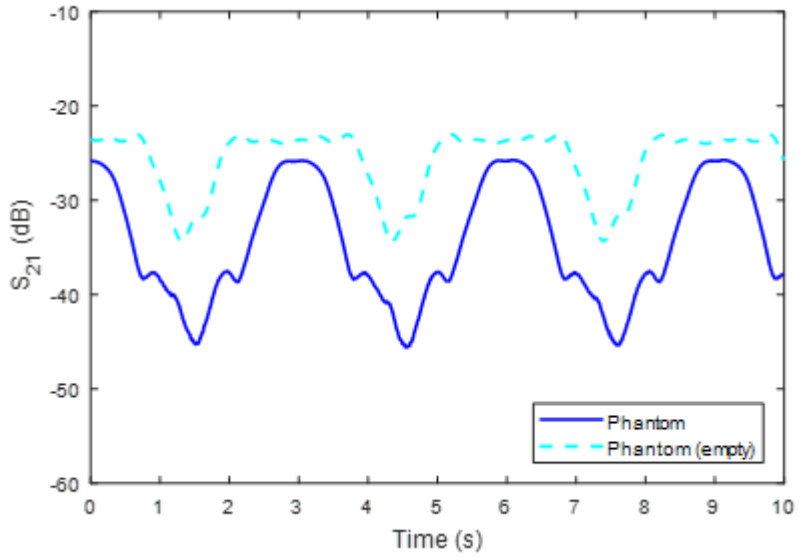

Figure 4.18. S_{21} vs time at 915MHz for the phantom filled with muscle tissue simulating solution and the empty phantom with monopole antennas on the chest/left wrist (back).

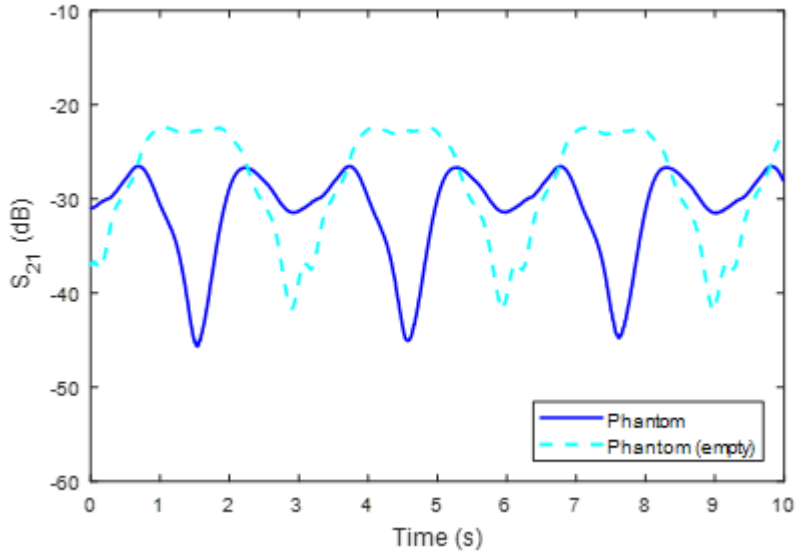

Figure 4.19. S_{21} vs time at 915MHz for the phantom filled with muscle tissue simulating solution and the empty phantom with monopole antennas on both wrists (front).

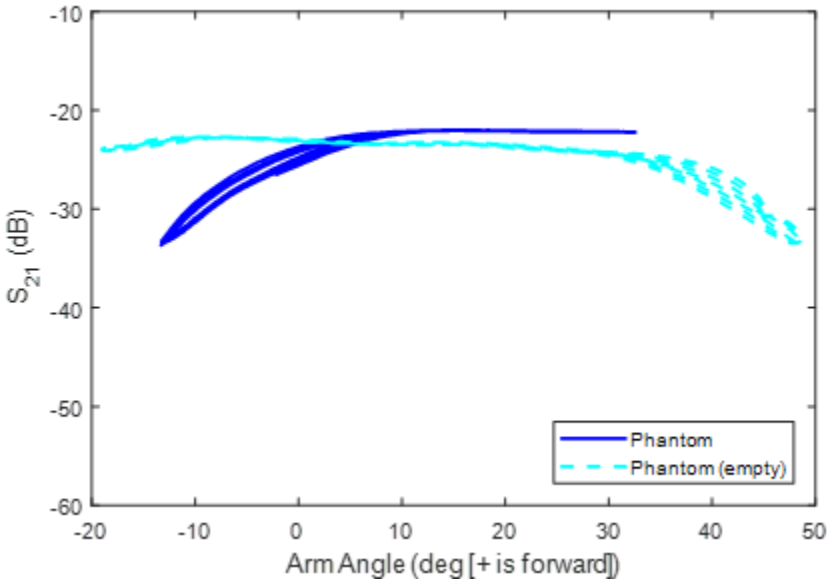

Figure 4.20. S_{21} vs angle at 915MHz for the phantom filled with muscle tissue simulating solution and the empty phantom with monopole antennas on the chest/left wrist (front).

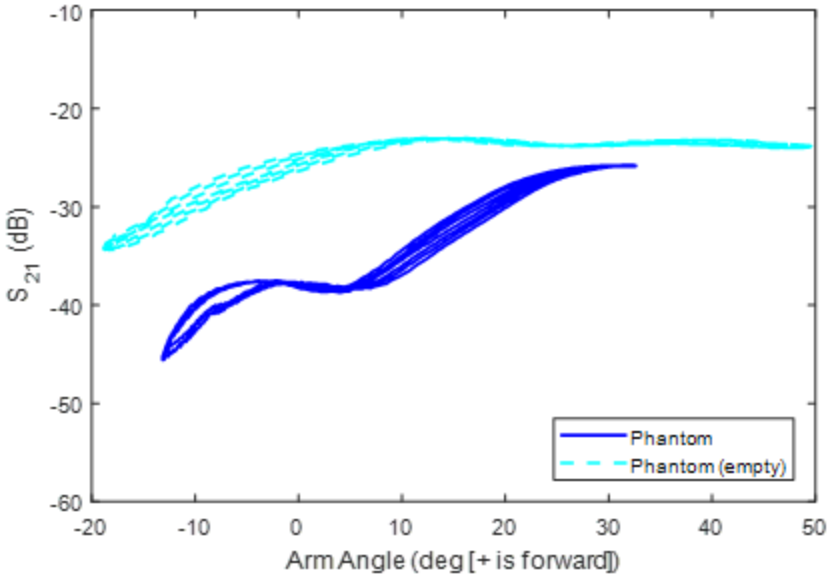

Figure 4.21. S_{21} vs angle at 915MHz for the phantom filled with muscle tissue simulating solution and the empty phantom with monopole antennas on the chest/left wrist (back).

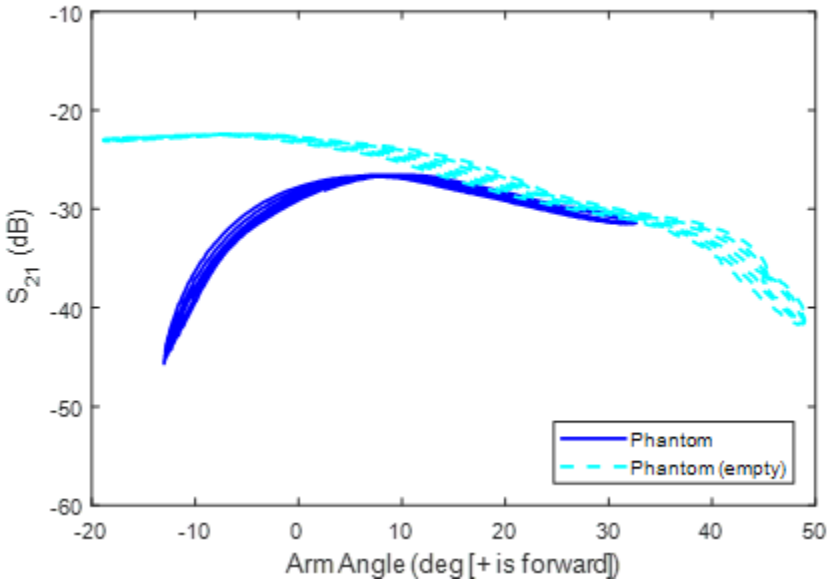

Figure 4.22. S_{21} vs angle at 915MHz for the phantom filled with muscle tissue simulating solution and the empty phantom with monopole antennas on both wrists (front).

Arm Swing Speed

Arm swing speed is another parameter of human body motion that can have a potential impact on on-body EM wave propagation. The arm swing speed effect is tested using the phantom model filled with water and a pair of 915MHz monopole antennas in the chest/left wrist (front) antenna configuration. The dielectric properties of the water are a permittivity of 42.9 and a conductivity of 2.39 at 915MHz. Two arm swing speeds were used, which were 2.5s and 3.0s.

Figure 4.23 shows average S_{21} vs average arm angle at 915MHz for the phantom at the 2.5s and 3.0s arm swing speeds with the chest/left wrist (front) antennas. Average S_{21} and average arm angle over eight cycles of arm swing data were plotted to reduce the slight variations in S_{21} per arm swing that the phantom model generates, making comparison between the two arm swing speeds clearer. The data shows that both arm swing speeds show the same overall S_{21} trend, with higher S_{21} occurring at positive arm

angles and lower S_{21} at negative arm angles. However, there is a shift when comparing the two arm swing speeds, where the S_{21} value will occur at an approximately 6deg different arm angle. For example, -30dB occurs at -16deg and -10deg for the 2.5s swing and at -10deg and -6 deg for the 3.0s swing. Another difference between the 2.5s arm swing speed and the 3.0s arm swing speed is the variation between the front and back swing. In Chapter 3, it was noted that the same arm angle can yield a different S_{21} value during a different phase of the arm swing, such as the arm moving forward compared to moving backwards. The variation in S_{21} is larger in the 2.5s arm swing speed than the 3.0s arm swing speed. For example, for the 2.5s arm swing speed, the max difference in S_{21} is 5.2dB at -7deg, compared to a max difference of 3.0dB at -8deg for the 3.0s arm swing speed. This suggests there is a potential arm swing speed effect, caused by the Doppler effect, in addition to the arm swing position effect that we have previously demonstrated; however, additional analysis on a larger data set and larger difference in speeds needs to be performed to determine statistical significance.

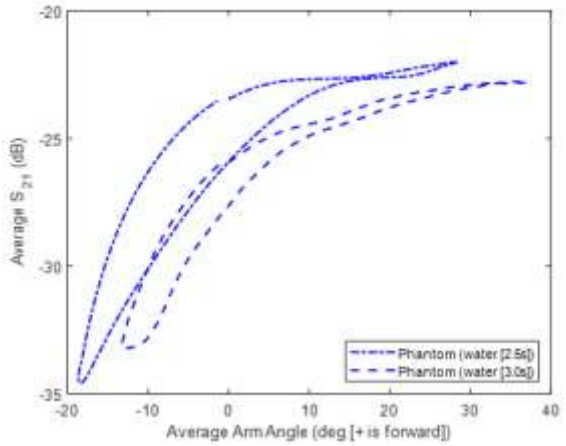

Figure 4.23. Average S_{21} vs average arm angle at 915MHz for the phantom model filled with water wearing monopole antennas on the chest/left wrist (front) at a 2.5s and 3.0s arm swing cadence.

Summary

A parametric study using the phantom model was performed. Four antenna and body parameters were tested, which were antenna operating frequency, antenna placement, body dielectric properties, and arm swing speed. The studies showed higher S_{21} at lower frequencies, changes in S_{21} fluctuation pattern with different antenna placements, large changes in S_{21} trends caused by body dielectric effects, and potential velocity directional effects on S_{21}. The phantom model also received further validation through comparison with human measurement for the antenna operating frequency and antenna placement studies.

CHAPTER FIVE

Antenna Types Testing Using the Phantom Model

Different antenna types have different sizes and form factors, which affect how practical they are in an actual WBAN implementation. For example, the monopole antenna is very reliable, but its form factor, even at high frequencies, can be inconvenient for someone to wear. A metal wire coming out of a person's watch or clothing can be difficult to maintain and is a potential safety hazard. The monopole could be covered, but that would still lead to a relatively noticeable protrusion. Other antenna types have the potential to be effective for on-body applications, while having improved form factors for wearable devices.

The antenna types tested are a monopole antenna, microstrip patch antenna, and an e-textile antenna. The monopole consists of a steel ground with a copper wire monopole, which can be seen in Figure 3.1. Despite the monopole antenna's shape being obtrusive when worn on the body, the monopole must be considered due to its strong antenna transmission when compared with other antenna types [7]. The microstrip patch antenna consists of a flat plate with a ground plane and antenna patch, which can be seen in Figure 5.1. The antenna tested operates at 915MHz. The antenna ground plane is made of FR-4 and the copper patch is 97.68mm by 76.53mm. The microstrip antenna was designed in CST simulation before fabrication to ensure the antenna design would properly resonate at 915MHz once fabricated. The CST simulation model of the microstrip antenna can be seen in Figure 5.2. The e-textile antenna is a dipole made of

conductive thread, which can be seen in Figure 5.3, and operates at 2GHz. The microstrip patch antenna and the e-textile antenna represent lower profile antenna choices that have greater potential for real-world wearable antenna applications. The microstrip patch antenna is a flat plate that could potentially be placed on some sort of band worn on the body without protruding too much. The e-textile antenna could be integrating into clothing, which would further reduce any interference the antenna could have on daily life. The monopole antenna serves as a useful baseline for comparison with these potential low-profile options to see how the antenna signal during motion is affected by using different types of antenna. The antennas are tested using the chest and left wrist (front), chest and left wrist (back), and both wrists (front) antenna placements. The antennas are tested using the phantom model filled with muscle tissue simulation solution and two human volunteers.

Figure 5.1. A 915MHz microstrip patch antenna with coaxial edge feed.

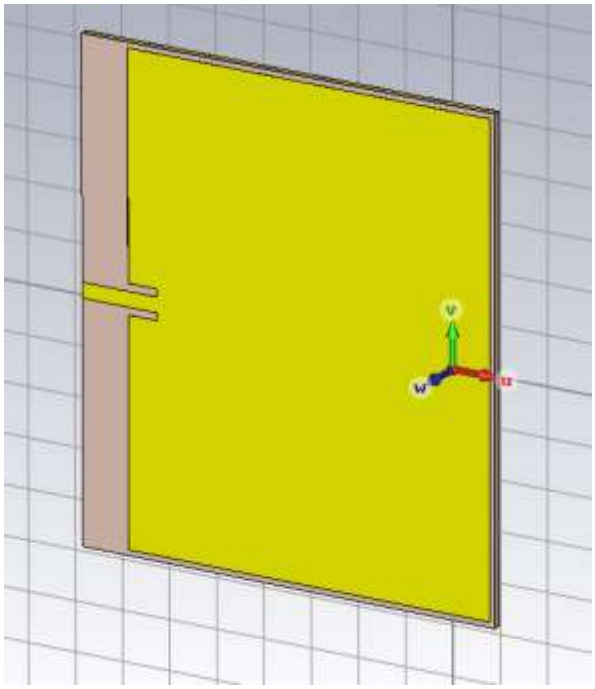

Figure 5.2. A 915MHz microstrip patch antenna in CST.

Figure 5.3. A 2.0GHz e-textile dipole antenna with coaxial feed.

The antenna reflection coefficients were verified by having S_{11} measured while the antenna was worn on a human chest. Figure 5.4 shows S_{11} vs frequency for the microstrip antenna. The reflection coefficient is shown to be below -10dB at 915MHz, which verifies that the antenna resonates at the target frequency on the human body. Figure 5.5 shows S_{11} vs frequency for the e-textile antenna. The reflection coefficient is shown to be below -10dB at 2GHz, which verifies that the antenna resonates at the target frequency on the human body. This reflection coefficient check allows for these antennas to be used in the dynamic human motion cases in this study.

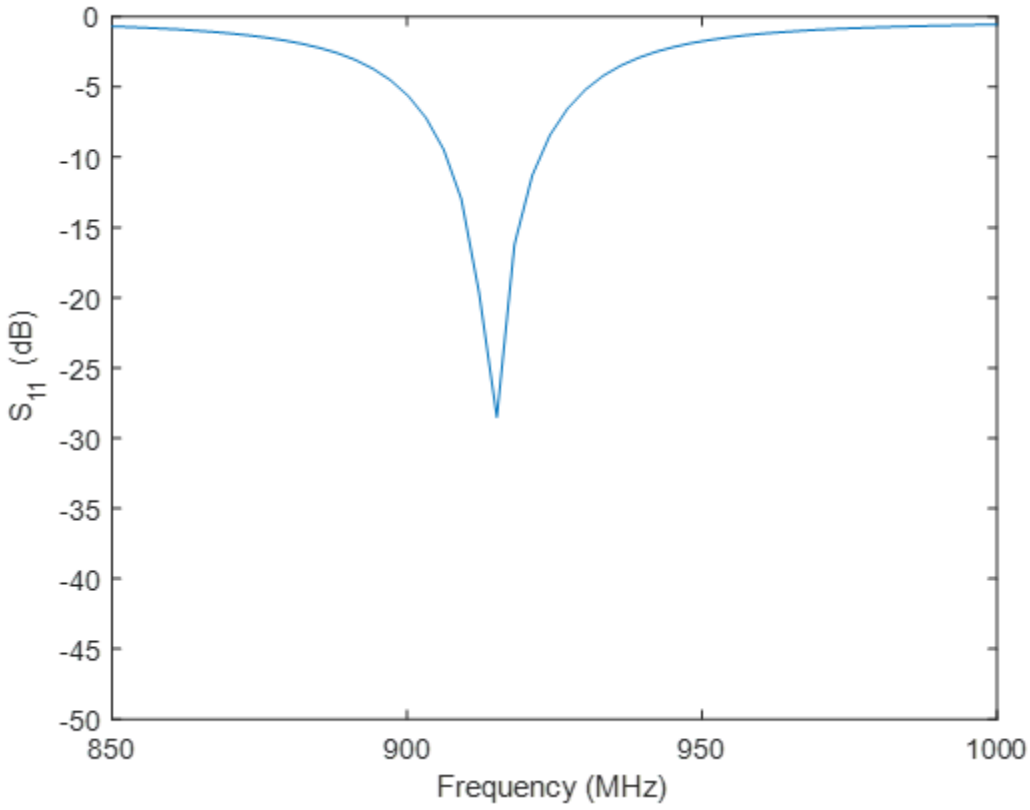

Figure 5.4. S_{11} vs frequency for the 915MHz microstrip antenna when worn on a human volunteer chest.

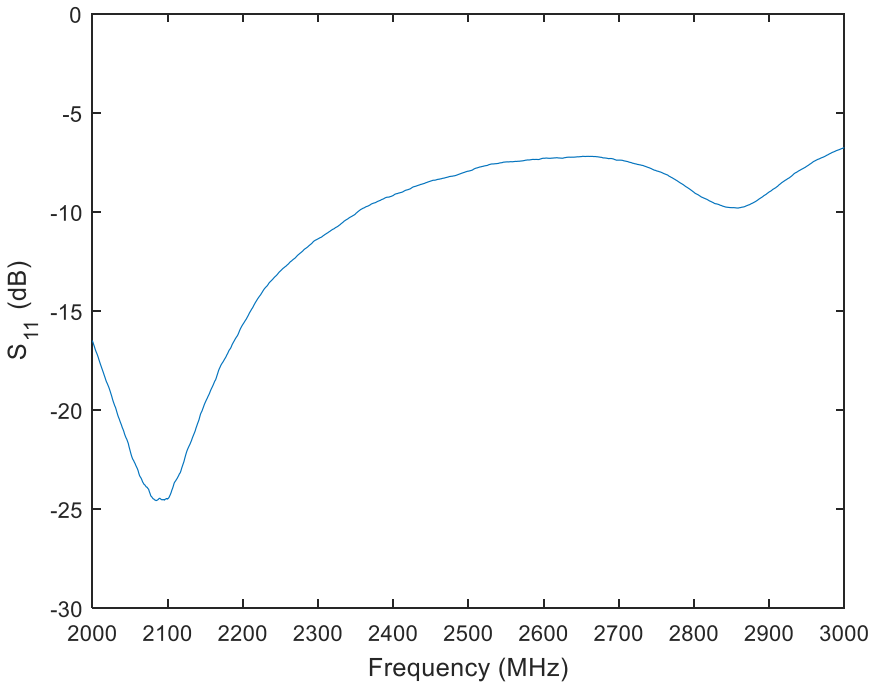

Figure 5.5. S_{11} vs. frequency for the 2.45GHz e-textile antenna when worn on a human volunteer chest.

A comparison of the sizes of the phantom model and the human volunteer can be seen in Table 5.1. The phantom model performed single arm swings at a 3s cadence with similar arm swing ranges as the human volunteers. The human volunteer performed a single arm swing motion at a 3s cadence following a metronome.

Table 5.1. Comparison of phantom and human volunteer size for microstrip and e-textile testing.

Body Part	Phantom Model	Human Volunteer
Torso Length (cm)	53.7	55
Torso Circumference (cm)	102.9	92.7
Arm Length (cm)	68.6	56
Arm Circumference (cm)	33	27.5

The Vicon passive motion capture system and markers were used to record motion data for both the phantom model and the human volunteers. The passive marker system aided in attaching the antennas to the human volunteers without potential stretching of the motion capture suit affecting the antenna placement due to the shape of the antenna affecting the coaxial connection points. The Phasespace motion capture suit aided in antenna placement for the monopole antennas due to fixed attachment points on the suit. In the case of the microstrip and e-textile antennas, the passive motion capture for both the phantom and human volunteers allowed for improved antenna placement for the human volunteers.

Both the phantom model and human volunteers perform an arm swinging motion and wear the antennas in the three antenna configurations used in the monopole parametric study, which are chest/left wrist (front), chest/left wrist (back), and both wrists (front). The phantom model is filled with muscle tissue simulation solution, with the dielectric properties listed in Table 2. The microstrip antenna results will be discussed, followed by the e-textile antenna.

Microstrip Antenna

Figure 5.6 shows S_{11} vs time at 915MHz for the wrist microstrip antenna worn on the phantom model in the chest/left wrist (front) antenna configuration. The plot shows that the S_{11} is consistently below -10dB for the duration of the motion activity. This shows that the antenna does not have any matching issues during the motion activity. There are S_{11} fluctuations with a periodicity that matches the cadence of the arm swing motion, which shows the motion does have a consistent effect on S_{11}. The S_{11} shows a

peak and dip pattern which consists of an M-shaped S_{11} peak (0.0s to 3.0s) followed by a dip period with minor fluctuations (2.0s to 3.0s), which repeats with each arm swing.

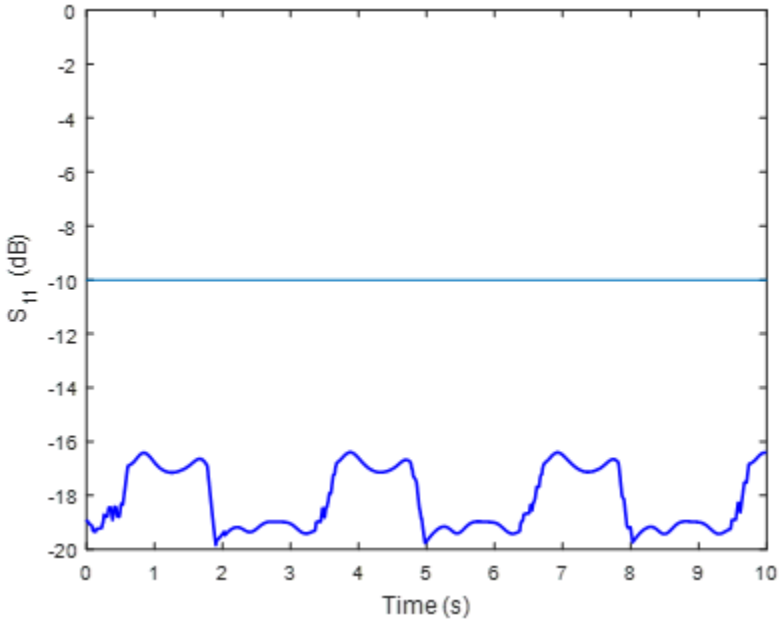

Figure 5.6. Wrist antenna S_{11} vs. time at 915MHz for the phantom model with microstrip antennas on the chest/left wrist (front).

CST simulation of the phantom model wearing microstrip antennas is used to verify the phantom model measurement. CST simulation of the phantom model is performed at 915MHz with the microstrip antenna. The scenario simulated uses the single arm swing with the antennas placed on the chest and left wrist (front), aligned to match the microstrip patch antenna alignment from the measurement. The simulation is performed at a mesh density of 30 lines per wavelength, resulting in significant simulation times using our current computing resources. Simulation times are generally over eight hours per frame of motion for this simulation scenario. The simulation uses motion capture data to move the phantom model's arm, using motion capture data at

10fps, which is sufficient to see the S_{21} fluctuation pattern caused by the phantom arm motion.

Figure 5.7 shows S_{21} vs time comparing the phantom model measurement with the phantom model simulation at 915MHz for the chest/left wrist (front) antenna configuration. There is generally good agreement between the measurement and simulation, where a similar peak and dip pattern can be seen. The peak and dip timing is also very similar. There are fluctuations within the S_{21} peaks and none in the S_{21} dips. The overall agreement between measurement and simulation again shows verification of phantom model's effect on EM wave propagation. The simulation was shifted by 8.5972dB so the average S_{21} of the measurement and simulation match.

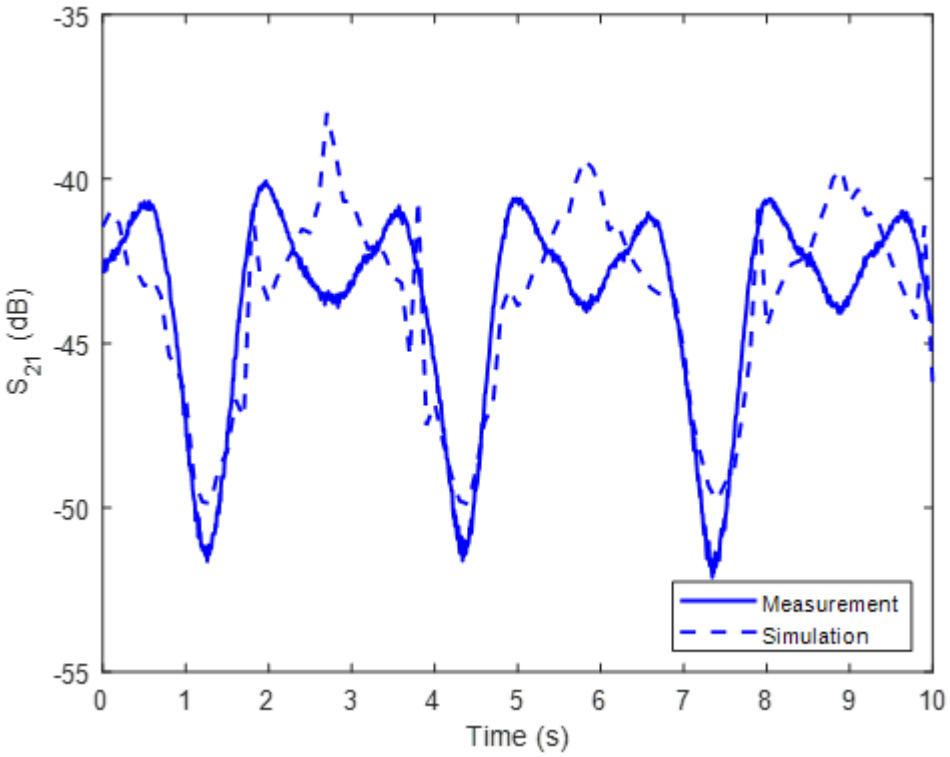

Figure 5.7. S_{21} vs. time at 915MHz for the phantom model measurement and phantom model simulation with microstrip antennas on the chest/left wrist (front).

Figure 5.8 shows S_{21} vs time comparing the phantom model measurement to the human volunteer measurement data for the microstrip antenna at 915MHz in the chest/left wrist (front) antenna configuration. Both the phantom model and human volunteer show a similar M-shaped peak and dip pattern during the arm swing motion. The periodicity is also similar between the phantom and human, with the peak and dips appearing during the same periods of time for the phantom and human. The range of magnitude is also similar, with only 3dB difference between range of S_{21} values for the human and phantom. The similarity between the phantom and human measurement shows that the phantom does have a similar effect on on-body EM wave propagation for the microstrip antenna in addition to the monopole antenna, which further suggests the phantom model is a tool capable of being used for a wide range of on-body EM wave propagation studies.

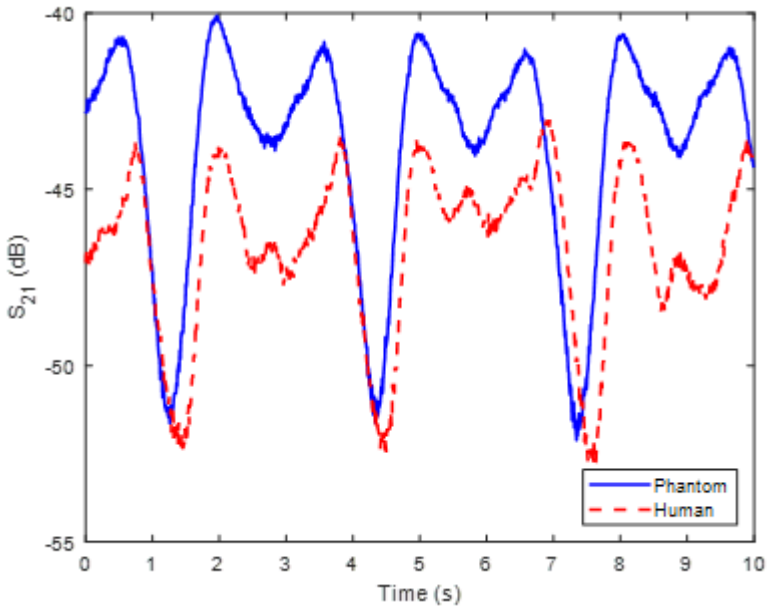

Figure 5.8. S_{21} vs. time at 915MHz for the phantom model measurement and human volunteer measurement with microstrip antennas on the chest/left wrist (front).

A comparison of results at 915MHz between the monopole antenna and the microstrip patch antenna shows that the two antenna types have similar on-body behavior. Figure 5.9 shows a comparison of the arm swinging motion with the antenna on chest and left wrist (front) at 915MHz for the phantom model with the bridge monopole and the microstrip patch antenna. A similar M-shaped peak and dip pattern and cadence can be seen for both antenna types on the phantom model. Both antennas show an M-shaped peak for a duration of approximately 2s followed by a sharp dip for approximately 1s. The ranges of magnitudes are also similar, with the microstrip antenna showing a range of 12.05dB and the monopole antenna showing a range of 11.69dB. The key difference between the two antenna types is the magnitude of S_{21} during the motion activity. The monopole antenna shows superior performance than the microstrip through its higher S_{21} during the entire range of motion. The microstrip antenna has an average S_{21} of -43.97dB and the monopole antenna has an average S_{21} of -25.04dB, which means the monopole antenna has an 18.93dB performance advantage over the microstrip antenna. The superior performance of the monopole antenna compared to the microstrip agrees with previous findings based on static human bodies [7]-[8] and is likely caused by the differences in polarization and radiation pattern between the antenna types [7]. Additionally, the difference in performance is unlikely due to antenna mismatch due to the confirmation of reflection coefficient seen in Figures 3.4 and 5.6.

Figure 5.10 shows S_{21} vs time for the phantom model with monopole and microstrip antenna for the chest and left wrist (back) configuration at 915MHz for the arm swinging motion. Both antenna types share a similar pattern and periodicity, which consists of a peak and dip pattern that occurs with similar timing. However, there is a

larger discrepancy in range of magnitude when compared to Figure 5.9. The range of magnitude for the microstrip is 5.65dB and the range of magnitude for the monopole is 19.83dB. As with Figure 5.9, the results in Figure 5.10 show the monopole has superior performance when compared to the microstrip, with higher S_{21} throughout the arm swing.

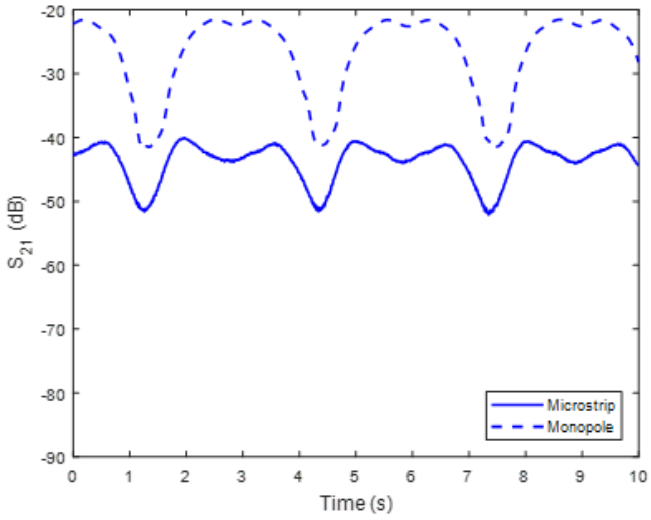

Figure 5.9. S_{21} vs. time at 915MHz for the phantom model measurement with microstrip antennas and monopole antennas on the chest/left wrist (front).

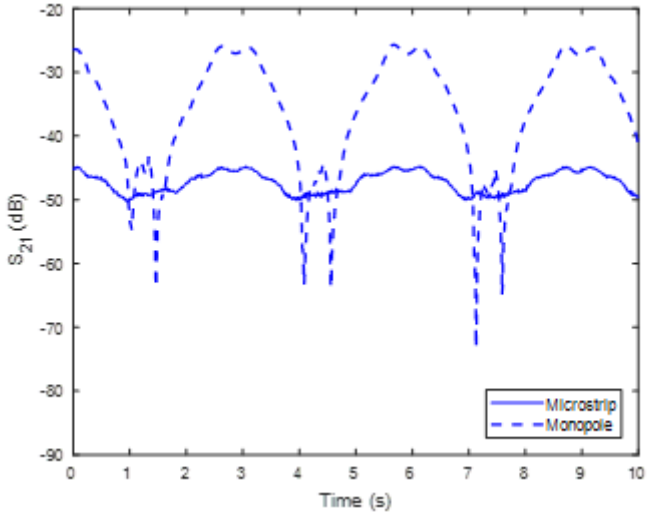

Figure 5.10. S_{21} vs. time at 915MHz for the phantom model measurement with microstrip antennas and monopole antennas on the chest/left wrist (back).

Figure 5.11 shows S_{21} vs time the phantom model with monopole and microstrip antenna for the both wrists (front) configuration at 915MHz for the arm swinging motion. Both antenna types share a similar M-shaped peak and dip pattern that have the same periodicity during the motion activity. The monopole antenna is shown to have consistently higher S_{21} than the microstrip during the entire motion activity.

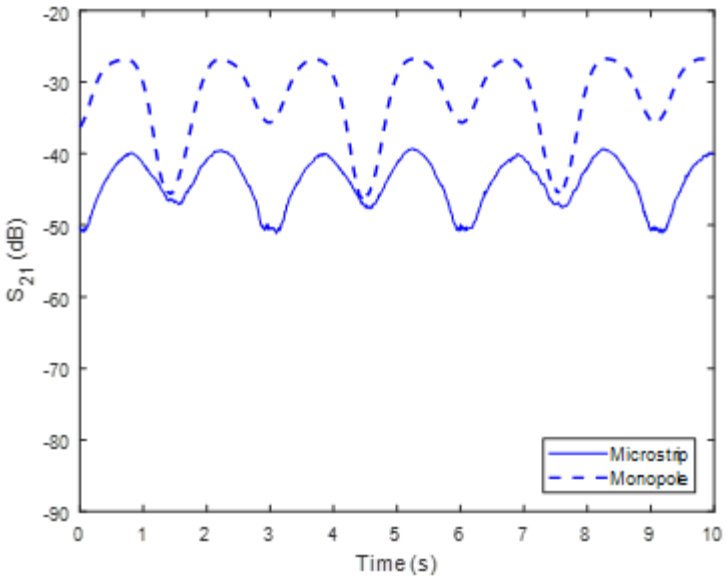

Figure 5.11. S_{21} vs. time at 915MHz for the phantom model measurement with microstrip antennas and monopole antennas on both wrists (front).

Figure 5.12 shows S_{21} vs angle for the phantom model and human volunteer with microstrip antennas for the chest and left wrist (front) configuration at 915MHz for the arm swinging motion. The phantom and human share a similar curve-shaped pattern that shows positive arm angles having the higher S_{21} values when compared to negative arm angles, though the peak S_{21} values occur around 10deg. This shows the antenna transmission for the microstrip is strongest when the arm is in front of the body (shoulder flexed). The similarity between the phantom and human becomes clearer when using the

arm angle to compare because the similarity in S_{21} vs angle further confirms that the phantom motion has a similar effect on antenna performance as human motion.

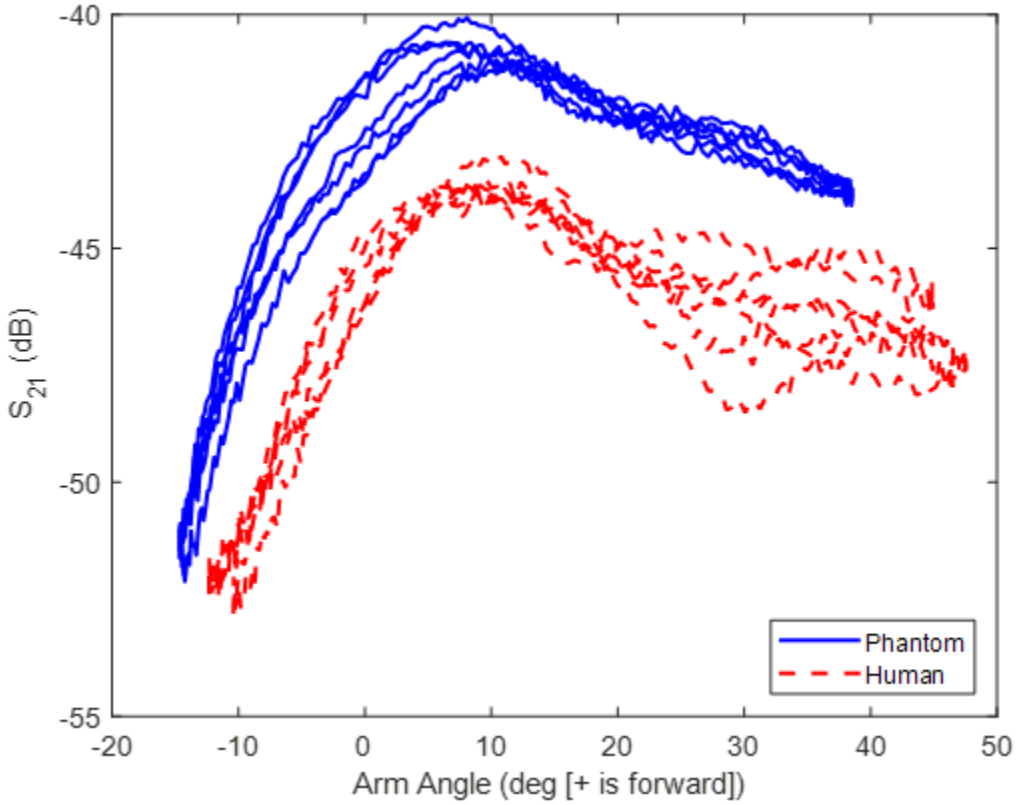

Figure 5.12. S_{21} vs arm angle at 915MHz for phantom model measurement and human volunteer measurement with microstrip antennas on the chest/left wrist (front).

Figure 5.13 shows S_{21} vs angle for the phantom model with monopole and microstrip antenna for the chest and left wrist (front) configuration at 915MHz for the arm swinging motion. This comparison also shows the similar pattern caused by motion, where S_{21} is lowest at negative arm angles and increases as the arm moves forward in front of the body. This suggests the body motion of the phantom has a similar impact on the antenna signal transmission of both antenna types. However, despite the similar S_{21} fluctuation pattern, there is a still a significant difference in magnitude between the two

antenna types, with the microstrip patch antenna seeing 18.93dB more loss than the monopole antenna.

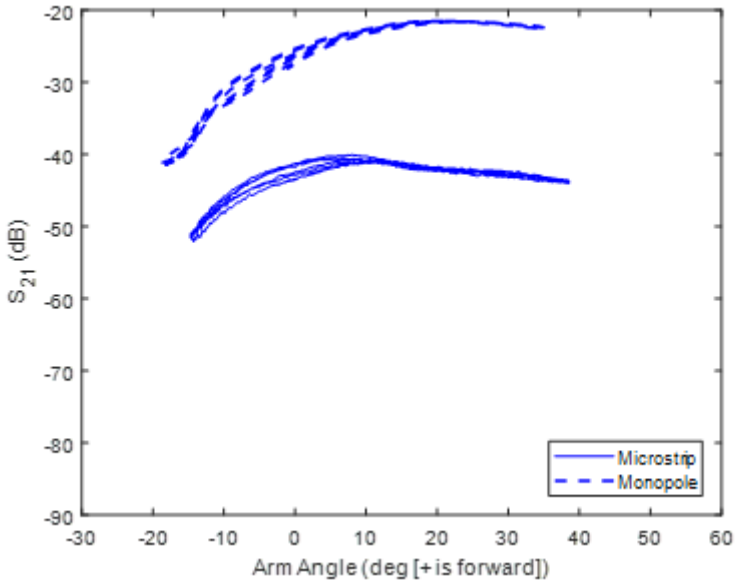

Figure 5.13. S_{21} vs. arm angle at 915MHz for the phantom model measurement with microstrip antennas and monopole antennas on the chest/left wrist (front).

Figure 5.14 shows S_{21} vs angle for the phantom model with monopole and microstrip antenna for the chest and left wrist (back) configuration at 915MHz for the arm swinging motion. Both antenna types share the trend of having higher S_{21} at positive arm angles, which means both antenna types have better antenna transmission when the arm is in front of the body. The plot also shows that S_{21} is higher at all arm angles for the monopole, which shows superior performance for the monopole.

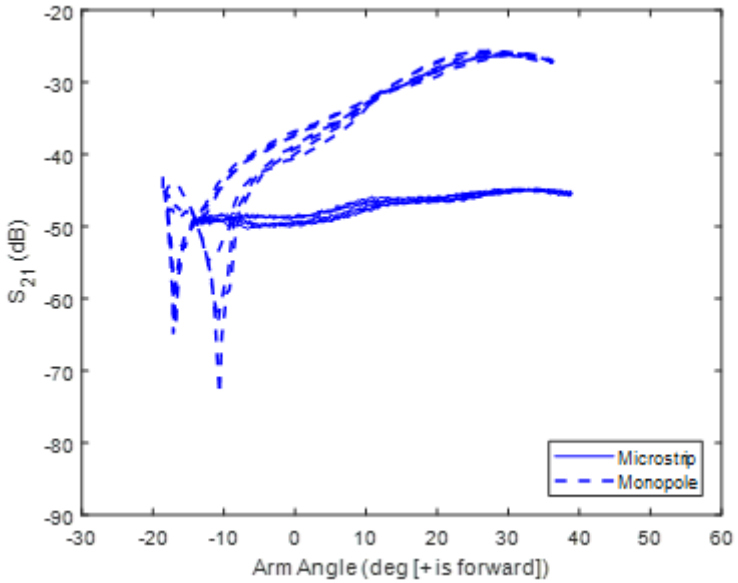

Figure 5.14. S_{21} vs. arm angle at 915MHz for the phantom model measurement with microstrip antennas and monopole antennas on the chest/left wrist (back).

Figure 5.15 shows S_{21} vs angle for the phantom model with monopole and microstrip antenna for the both wrists (front) configuration at 915MHz for the arm swinging motion. While the two antenna types have a similar curve-shaped pattern for S_{21} vs angle, the monopole and microstrip have differences in S_{21} performance trends. The microstrip shows a trend of having lower S_{21} at high (over 30deg) positive arm angles, while the monopole shows overall higher S_{21} at positive arm angles. S_{21} is higher for the monopole throughout the arm swing, though S_{21} is similar at arm angles below -10deg. This shows the monopole also has superior performance in this antenna configuration. The overall superior performance of the monopole for all three antenna configurations suggests the monopole is better suited for on-body applications in terms of antenna performance; however, the form factor of the antenna does not work well for practical everyday use in on-body scenarios.

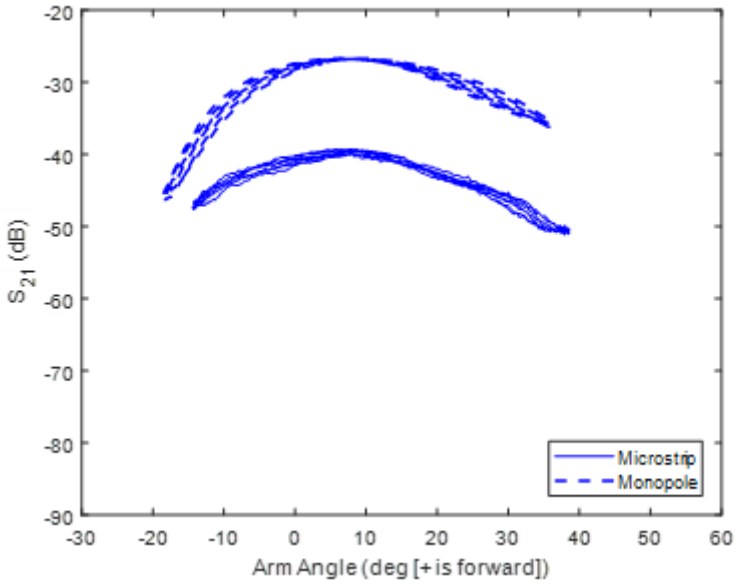

Figure 5.15. S_{21} vs. arm angle at 915MHz for the phantom model measurement with microstrip antennas and monopole antennas on both wrists (front).

E-Textile Antenna

Figure 5.16 shows S_{11} vs time at 2.45GHz for the wrist e-textile antenna worn on the phantom model in the chest/left wrist (front) antenna configuration. The S_{11} is consistently near-10dB on the wrist, showing overall resonance during the motion activity. However, there is more de-tuning than with the monopole and microstrip antennas, which stayed below -10dB at all times. The S_{11} shows fluctuation patterns with a periodicity matching the cadence of the arm swing motion. The confirmation that the e-textile antenna resonates properly at 2.45GHz allows for a fair comparison of antenna performance with a 2.45GHz monopole antenna.

Figures 5.17, 5.18, and 5.19 show S_{21} vs time comparing the monopole and e-textile antennas at 2.45GHz on the phantom model for the arm swinging motion. Figure 5.17 shows the chest/left wrist (front) antenna configuration, which shows there is a significant performance advantage for the monopole antenna as seen in the higher S_{21}

values. Additionally, both antenna types do show S_{21} fluctuations caused by the phantom's body motion, but the two antenna types do not show significant similarity when comparing against time. Figure 5.18 shows the chest/left wrist (back) antenna configuration, which shows higher overall S_{21} for the monopole antenna compared to the e-textile antenna. Both antenna types show a similar peak and dip pattern characterized by a peak period (2.75s to 3.25s) and an M-shaped dip period (3.25s to 5.75s). Figure 5.19 shows the both wrists (front) antenna configuration. Unlike the chest/left wrist (front) and chest/left wrist (back) antenna configurations, the S_{21} magnitude is very similar for both antenna types, which suggests that each antenna is differently affected by antenna placement, meaning an antenna that is strong is some scenarios may perform worse on different body placements. Both antennas also share similar peak and dip pattern timings.

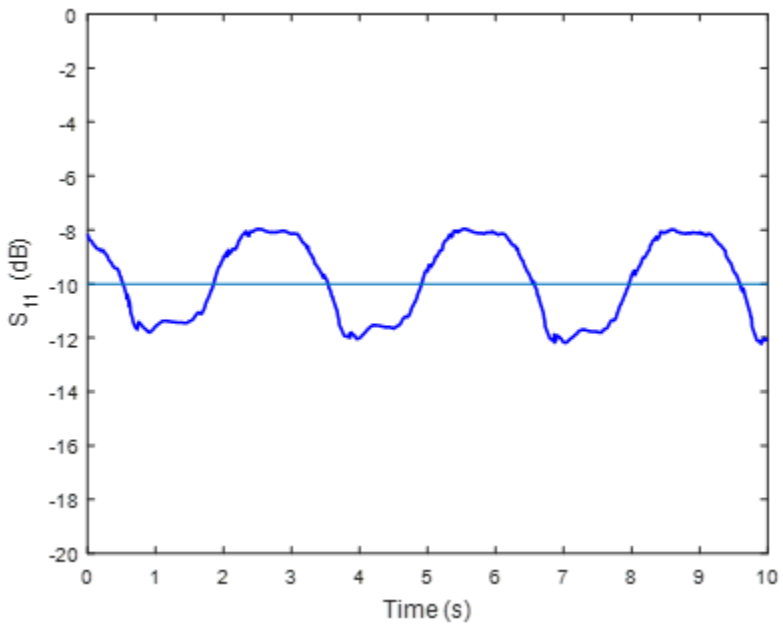

Figure 5.16. Wrist antenna S_{11} vs time at 2.45GHz for the phantom model wearing e-textile antennas on the chest/left wrist (front).

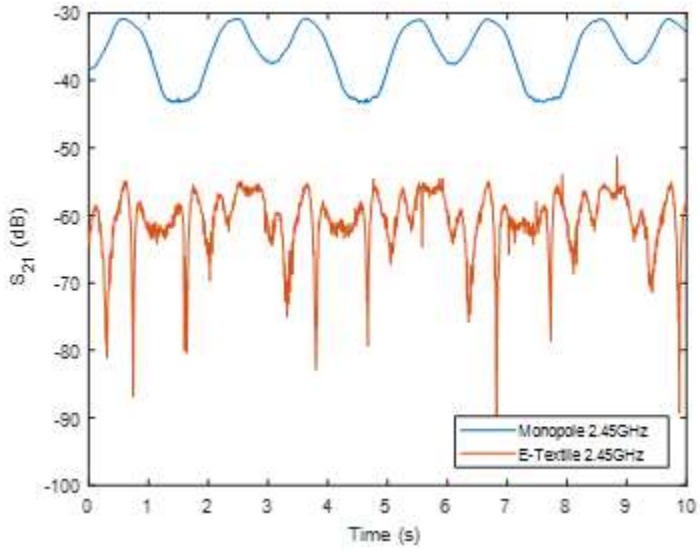

Figure 5.17. S_{21} vs time at 2.45GHz for the phantom model wearing monopole and e-textile antennas on the chest/left wrist (front).

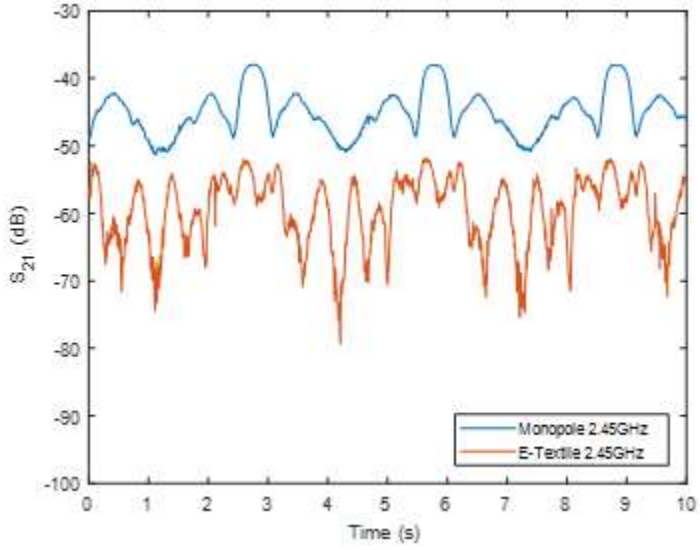

Figure 5.18. S_{21} vs time at 2.45GHz for the phantom model wearing monopole and e-textile antennas on the chest/left wrist (back).

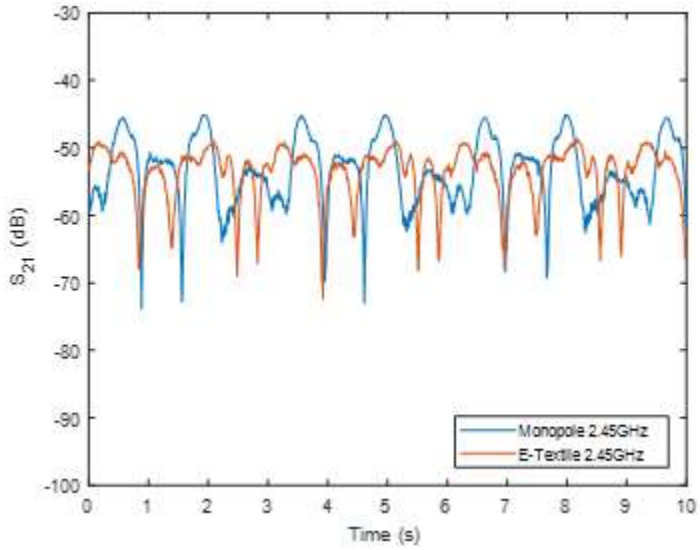

Figure 5.19. S_{21} vs time at 2.45GHz for the phantom model wearing monopole and e-textile antennas on both wrists (front).

Figures 5.20, 5.21, and 5.22 show S_{21} vs arm angle comparing the monopole and e-textile antennas at 2.45GHz on the phantom model for the arm swinging motion. Figure 5.20 shows the chest/left wrist (front) antenna configuration, which shows there is a significant performance advantage for the monopole antenna as seen in the higher S_{21} values at all arm angles. Both antennas share the trend of higher S_{21} at positive arm angles. Figure 5.21 shows the chest/left wrist (back) antenna configuration, which shows higher overall S_{21} for the monopole antenna compared to the e-textile antenna at all arm angles. Both antenna types show higher S_{21} at higher arm angles (over 20 deg), with lower arm angles yielding a lower and fairly plateaued S_{21}. Figure 5.22 shows the both wrists (front) antenna configuration, which shows similar S_{21} magnitude for both antenna types and a similar pattern of peak S_{21} values in the middle range of arm angles (-5 deg to 15 deg). Overall, the two antenna types show similarities in S_{21} pattern during motion for

some antenna configurations and relative antenna performance may be dependent on antenna placement.

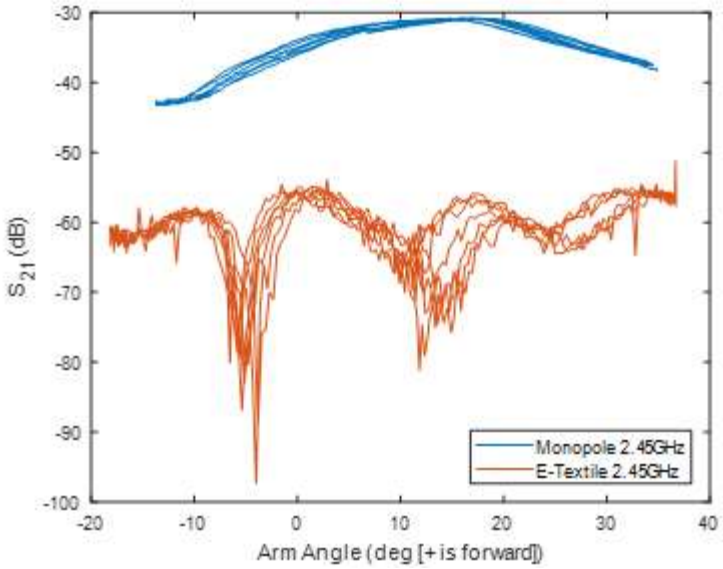

Figure 5.20. S_{21} vs angle at 2.45GHz for the phantom model wearing monopole and e-textile antennas on chest/left wrist (front).

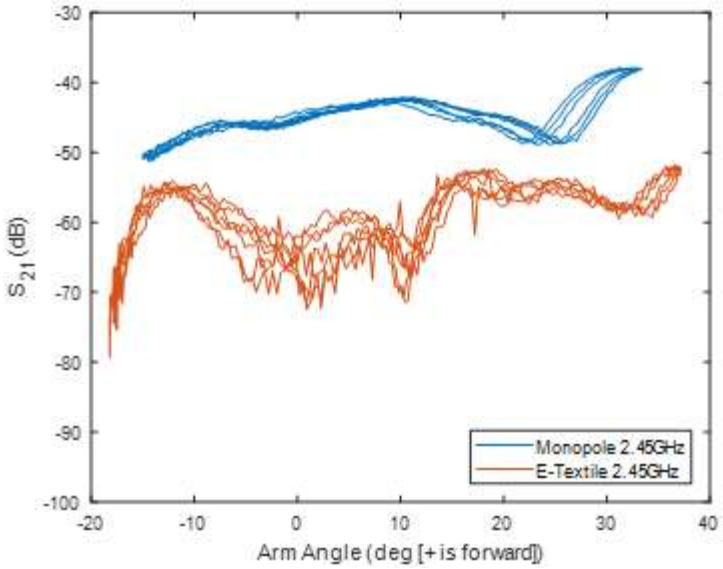

Figure 5.21. S_{21} vs angle at 2.45GHz for the phantom model wearing monopole and e-textile antennas on the chest/left wrist (back).

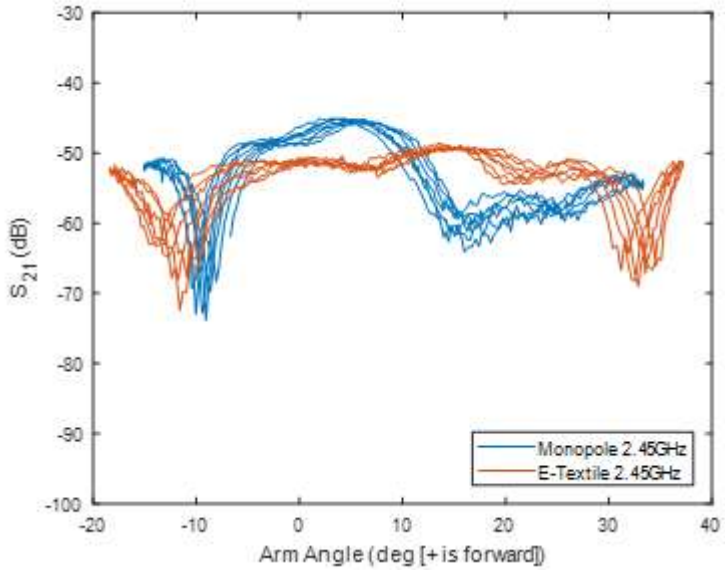

Figure 5.22. S_{21} vs angle at 2.45GHz for the phantom model wearing monopole and e-textile antennas on both wrists (front).

Summary

The phantom model was used to compare on-body antenna performance for monopole, microstrip, and e-textile antennas. Different antenna placements were assessed and were found to have a greater impact on S_{21} magnitude for the monopole antennas than the microstrip or e-textile. The antennas were shown to have generally similar S_{21} fluctuation patterns and the monopole antenna overall had the highest performance.

CHAPTER SIX

Conclusions and Future Work

Conclusions

The use of a human body phantom model has many benefits for the study of on-body EM wave propagation. This dissertation has developed a human body phantom model that is modular in design and has been validated through multiple methods. The use of motion capture to correlate body position with antenna performance, such as S_{11} and S_{21} provides valuable insight into the way human body motion affects on-body EM wave propagation. The motion capture data also allows for a simulation model to be created in CST that matches the phantom model motion, allowing for a direct comparison of phantom measurement and simulation to provide verification of the phantom model accuracy. The phantom model measurement is also compared with measurement from multiple human volunteers to verify the phantom model has a similar effect on on-body EM wave propagation during body motion. Both simulation and human measurement comparison showed similar pattern, periodicity, and magnitude to the phantom measurement, meaning the phantom model is useful for on-body EM wave propagation studies. A comparison of mean S_{21} difference between the phantom and human volunteers showed the discrepancy between phantom and human measurement was in a similar range as previous studies comparing human measurement to various types of computer models.

The verification of the phantom model allowed for a parametric study of various antenna and body parameters using the phantom model. Antenna operating frequency, antenna placement, body dielectric properties, and arm swing speed were tested. Higher operating frequencies were shown to have greater loss than lower frequencies. Different antenna placements showed different S_{21} fluctuation patterns, with antenna configurations sharing a wrist (front) antenna showing similar M-shaped fluctuations in S_{21}. Changes in dielectric properties showed a separate body and motion effect, which resulted in wrist (front) antenna configurations having reversed S_{21} trends due to changes in line-of-sight, wave scattering, and the creeping wave due to a lack of body effect. Arm swing speed shifts in antenna performance due to differences in velocity due to the Doppler effect. The parametric study shows the value of the phantom due to the ability to easily change body and antenna parameters, allowing for different factors to be studied in isolation.

The verified phantom model was used to test the performance of three antenna types, which were monopole, microstrip, and e-textile. The combination of motion capture and VNA data collection is utilized again to allow for comparison of body position with antenna transmission data. The phantom model showed superior monopole antenna performance compared to the microstrip and e-textile antennas for dynamic motion scenarios, which means additional antenna optimization is necessary. The phantom received further verification through agreement during comparison with human measurement and computer simulation when using multiple antenna types.

This study contributes to the study of on-body EM wave propagation by developing a phantom model approach that incorporates measurement and simulation that both utilize a motion capture approach to correlating body motion and position to antenna

performance. The phantom model is used for a variety of parametric studies that include more operating frequencies and human comparison than previous phantom studies and performs antenna type testing in dynamic motion scenarios, which generally have been performed on static bodies previously. Overall, the phantom model has been verified as a valuable tool for studying on-body EM wave propagation and on-body antenna design and testing. The findings from the parametric and antenna type studies can be used to guide future on-body antenna designs to account for factors, such as, optimal antenna placements and motion effects on EM wave propagation.

Future Works

The verification of the phantom model allows for in-depth study of the parameters that can affect EM wave propagation during human body motion scenarios. This knowledge can benefit the design process of on-body antenna for wearable devices, improving the performance and usability of WBAN systems for valuable applications, such as long-term, remote health monitoring.

Future work includes expanding the phantom model to allow for greater range of motion and adding lower-body segments to allow for analysis of leg motion. A study of the impact leg motion have on lower-body antenna would then be performed. Additionally, more data with additional human volunteers can be used for further validate the model and provide additional insight into the effect different body types can have on EM wave propagation. The study would involve a group of human volunteers of varying body mass index (BMI) to represent different body types and the phantom dielectric solution would be varied to represent having more muscle and having more fat. The

phantom model can also provide insight into simulation models to help improve agreement with measurement for more complex simulation models.

Finally, the phantom model will be used for additional on-body antenna design and optimization for WBAN applications. The phantom model simulation framework would be used to design different antennas, such as e-textile antennas or adaptive antennas. The antennas could then be fabricated and tested on the phantom model and compared with human volunteers using our measurement methods.

BIBLIOGRAPHY

[1] Z. Ullah, I. Ahmed, T. Ali, N. Ahmad, F. Niaz, and Y. Cao, "Robust and Efficient Energy Harvested-Aware Routing Protocol With Clustering Approach in Body Area Networks," IEEE Access, vol. 7, March 2019.

[2] A. Weiss, T. Herman, N. Giladi, and J. Hausdorff, "Objective assessment of fall risk in Parkinson's disease using a body-fixed sensor worn for 3 days," PLos One, vol. 9, no. 5, pp. 1-10, May 2014.

[3] A. Ibrahim and M. Younis, "Simple fall criteria for MEMS sensors: data analysis and sensor concept," Sensors, vol. 14, no. 7, pp. 12149-12173, July 2014.

[4] E. Fortune, V. Lugade, M. Morrow, and K. Kaufman, "Validity of using tri-axial accelerometers to measure human movement – Part II: Step counts at a wide range of gait velocities," Medical Engineering & Physics, vol. 36, pp. 659-669, 2014.

[5] S. Tan, J. García-Guzmán, and F. Villa-López, "A wireless body area network for pervasive health monitoring within smart environments," 2012 IEEE Second International Conference on Consumer Electronics – Berlin, 2012.

[6] H. Sabti and D. Thiel, "Time multiplexing-star shape body sensor network for sports applications," 2014 IEEE Antennas and Propagation Society International Symposium, July 2014.

[7] P. Hall and Y. Hao, Antennas and Propagation for Body-Centric Wireless Communications, 2nd ed. Norwood, MA, USA: Artech House, 2012, ch. 3, pp. 63-106.

[8] G. Conway and W. Scanlon, "Antennas for Over-Body-Surface Communication at 2.45GHz," IEEE Transactions on Antennas and Propagation, vol. 57, no. 4, pp. 884-855, April 2009.

[9] M. Li, W. Lou, and K. Ren, "Data security and privacy in wireless body area networks," IEEE Wireless Communications, vol. 17, no. 1, pp. 51- 58, February, 2010.

[10] M. Kumar, "Security Issues and Privacy Concerns in the Implementation of Wireless Body Area Network," 2014 International Conference on Information Technology, December 2014.

[11] I. Sawaneh, I. Sankoh, and D. Koroma, "A survey on security issues and wearable sensors in wireless body area network for healthcare system," 2017 14th International Computer Conference on Wavelet Active Media Technology and Information Processing, December 2017.

[12] D. Xue, T. Liller, B. Garner, and Y. Li, "Simulation and measurement of on-body wave propagation," 2014 Texas Symposium on Wireless and Microwave Circuits and Systems, April 2014.

[13] S. Cotton and W. Scanlon, "An experimental investigation into the influence of user state and environment on fading characteristics in wireless body area networks at 2.45GHz," IEEE Transactions on Wireless Communications, vol. 8, no. 1, January 2009.

[14] A. Taparugssanagorn, B. Zhen, R. Tesi, M.Hämäläinen, J. Iinatti, and R. Kohno, "A UWB WBAN channel model based on pseudo-dynamic measurement," annals of telecommunications, vol. 66, no. 3-4, pp. 177-185, April 2011.

[15] M. Munoz, R. Foster, and Y. Hao, "Exploring Physiological Parameters in Dynamic WBAN Channels," IEEE Trans. on Ant. and Prop., vol. 62, no. 10, pp. 5268-5281, October 2014.

[16] K. Li, K. Honda, and K. Ogawa, "Shadow-Fading BER Characterization of BAN Antennas Based on Realistic Walking Models," 2013 7th International Symposium on Medical Information and Communication Technology, March 2013.

[17] Ł, Januszkiewicz and S. Hausman, "Simplified Human Phantoms for Wireless Body Area Network Modelling," 2015 9th European Conference on Antennas and Propagation (EuCAP), April 2015.

[18] N. Yamamoto, N. Shirataka, D. Kobayashi, K. Honda, and K. Ogawa, "BAN Radio Link Characterization Using an Arm-Swinging Dynamic Phantom Replicating Human Walking Motion," IEEE Trans. On Ant. And Prop., vol. 61, no. 8, pp. 4315-4326, August 2013.

[19] K. Li, K. Honda, and K. Ogawa, "Rice Channel Realization for BAN Over-The-Air Testing Using a Fading Emulator with an Arm-Swinging Dynamic Phantom," IEICE Trans. Commun., vol. E98-B, no. 4, April 2015.

[20] K. Ogawa, K. Li, and K. Honda, "BAN Over-the-Air testing using an arm-swinging dynamic phantom," 2013 IEEE MTT-S International Microwave Workshop Series on RF and Wireless Technologies for Biomedical and Healthcare Applications, December 2013.

[21] S. Swaisenyakorn, S. Kelly, and J. Batchelor, "A study of factors affecting wrist channel characteristics for walking postures using motion capture," IEEE Trans. on Ant. and Prop., vol. 62, no. 4, pp. 2231-2237, January 2014.

[22] K. Li, Z. Nie, Y. Liu, L. Wang, and Y. Hao, "Evaluation of Propagation Characteristics Using the Human Body as an Antenna," Sensors, vol. 17, 2017.

[23] Iswandi, T. Aoyagi, M. Kim, and J. Takada, "The utilization of body skeleton model for modeling the dynamic BAN channels," Sixth European Conf. on Antennas and Propagation, March 2012.

[24] P. Hall, Y. Hao, Y. Nechayev, A. Alomainy, C. Constantinou, C. Parini, M. Kamarudin, T. Salim, D. Hee, R. Dubrovka, A. Oswadally, W. Song, A. Serra, P. Nepa, M. Gallo, and M. Bozzetti, "Antennas and Propagation for On-Body Communication Systems," IEEE Antennas and Propagation Magazine, vol. 49, no. 3, pp. 41-58, June 2007.

[25] M. Gallo, P. Hall, Q. Bai, Y. Nechayev, C. Constantinou, and M. Bozzetti, "Simulation and measurement of dynamic on-body communication channels," IEEE Trans. On Ant. And Prop., vol. 59, no. 2, February 2011.

[26] C. Oliveira, M. Mackowiak, and L. Correia, "A Comparison of Phantom Models for On-Body Communications," 2012 IEEE 23rd Symposium on Personal, Indoor and Mobile Radio Communications – (PIMRC), 2012.

[27] T. Aoyagi, Iswandi, M. Kim, J. Takada, K. Hamaguchi, and R. Kohno, "Body motion and channel response of dynamic body area channel," Proceedings of the 5th European Conference on Antennas and Propagations, April 2011.

[28] G. Conway, W. Scanlon, S. Cotton, and M. Bentum, "An Analytical Path-Loss Model for On-Body Radio Propagation," 2010 URSI International Symposium on Electromagnetic Theory, 2010.

[29] L. Liu, F. Keshmiri, C. Craeye, P. Dr Doncker, and C. Oestges, "An Analytical Modeling of Polarized Time-Variant On-Body Propagation Channels with Dynamic Body Scattering," EURASIP Journal on Wireless Communications and Networking, January 2011.

[30] D. Kurup, G. Vermeeren, E. Tanghe, W. Joseph, and L. Martens, "In-to-Out Body Antenna-Independent Path Loss Model for Multilayered Tissues and Heterogeneous Medium," Sensors, vol. 15, 2015.

[31] L. Chevalier, S. Sahuguède, and A. Julien-Vergonjanne, "Wireless Optical technology based Body Area Network for health monitoring application," 2015 IEEE International Conference on Communications, June 2015.

[32] R. Chandra and A. Johansson, "An elliptical analytical loss model for wireless propagation around the human torso," 2012 6th European Conference on Antennas and Propagation, March 2012.

[33] D. Xue, B. Garner, and Y. Li. "Investigation of 433MHz and 915MHz On-Body Wave Propagations," 2015 Texas Symposium on Wireless and Microwave Circuits and Systems, April 2015.

[34] G. Lee, B. Garner, and Y. Li, "Simulation and measurement of electromagnetic wave propagation on dynamic human bodies," IET Microwaves, Antennas & Propagation, vol. 11, no. 10, pp. 1347-1353, August 2017.

[35] Advanced MRI, National Institutes of Health, "Dielectric phantom recipe generator," [Online] Available: https://amri.ninds.nih.gov/cgi-bin/phantomrecipe [Accessed: Dec. 14, 2018]

[36] Federal Communications Commission, "Body Tissue Dielectric Parameters," [Online] Available: https://www.fcc.gov/general/body-tissue-dielectric-parameters [Accessed: Dec. 14, 2018]

[37] ITU Radio Regulations, [Online] Available: https://www.itu.int/net/ITU R/terrestrial/faq/index.html [Accessed: Feb 20, 2020]